

A MICROFLUIDIC SYSTEM FOR DIELECTROPHORETIC
CHARACTERIZATION OF CANCER CELLS

A THESIS SUBMITTED TO
THE GRADUATE SCHOOL OF NATURAL AND APPLIED SCIENCES
THE MIDDLE EAST TECHNICAL UNIVERSITY
BY

KAAN SEL

IN PARTIAL FULFILLMENT OF THE REQUIREMENTS FOR THE DEGREE OF
MASTER OF SCIENCE
IN
THE DEPARTMENT OF ELECTRICAL AND ELECTRONICS ENGINEERING

JULY 2018

Approval of the thesis:

**A MICROFLUIDIC SYSTEM FOR DIELECTROPHORETIC CHARACTERIZATION OF
CANCER CELLS**

Submitted by **KAAN SEL** in partial fulfillment of the requirements for the degree of **Master of Science in Electrical and Electronics Engineering Department, Middle East Technical University** by,

Prof. Dr. Halil Kalıpcılar
Dean, Graduate School of **Natural and Applied Sciences**

Prof. Dr. Tolga Çiloğlu
Head of Department, **Electrical and Electronics Engineering**

Prof. Dr. Haluk K lah
Supervisor, **Electrical and Electronics Eng. Dept., METU**

Examining Committee Members:

Prof. Dr. Tayfun Akın
Electrical and Electronics Engineering Dept., METU

Prof. Dr. Haluk K lah
Electrical and Electronics Engineering Dept., METU

Asst. Prof. Dr. Serdar Kocaman
Electrical and Electronics Engineering Dept., METU

Asst. Prof. Dr. Kıvanç Azgın
Mechanical Engineering Dept., METU

Assoc. Prof. Dr. Ender Yıldırım
Mechanical Engineering Dept., Cankaya University

Date: 18.07.2018

I hereby declare that all information in this document has been obtained and presented in accordance with academic rules and ethical conduct. I also declare that, as required by these rules and conduct, I have fully cited and referenced all material and results that are not original to this work.

Name, Last name : Kaan Sel

Signature : _____

ABSTRACT

A MICROFLUIDIC SYSTEM FOR DIELECTROPHORETIC CHARACTERIZATION OF CANCER CELLS

Sel, Kaan

M. Sc., Department of Electrical and Electronics Engineering
Supervisor: Prof. Dr. Haluk Klah

June 2018, 73 pages

Dielectrophoresis (DEP) is a promising cell manipulation approach for early diagnosis of cancer, which significantly increases chances of successful treatment. Compared to other cell manipulation techniques that rely on surface antigens, DEP systems enable label-free, cost-effective, simply-implementable cell characterization and separation. However, separation efficiency of the DEP based systems is limited and still far from meeting the medical requirements for early cancer detection. In order to improve the throughput of current DEP systems, it is important to obtain the optimum operating conditions. The main objective of this thesis is to conduct accurate dielectrophoretic characterization of cancer cells without ascertaining cell dielectric properties at different operating conditions in autonomous fashion.

The presented system integrates a microfluidic DEP device with a CMOS image sensor, and a portable signal generator. The system enables DEP spectra analysis of cells in a wide frequency band (30 kHz to 50 MHz). The microfluidic DEP device, contains optimized electrode structures that can generate isomotive electric-field inside the analysis region. Hence, cell motion under the DEP force can directly be related to its dielectrophoretic behaviour. In addition, post-processing can be done either in a custom-developed MATLAB GUI or in a custom-developed Android software connected to a smartphone using an automated cell tracking algorithm.

With the DEP characterization device presented in this thesis, different conditions (operating frequency, medium characteristics) can be tested in a portable, autonomous and rigorous fashion to find the optimum case for cell separation. The system was tested with both MFC-7 (Human Breast Adenocarcinoma) and K562 (Human Chronic Myeloid Leukemia) cells due to availability. The results display consistency with the DEP spectrum studies conducted with these two cell groups in the literature.

Keywords: Dielectrophoresis (DEP), cell dielectric characterization, single-cell analysis, BioMEMS, isomotive electric-field

ÖZ

KANSER HÜCRELERİNİN DİELEKTROFORETİK KARAKTERİZASYONU İÇİN MİKROAKIŞKAN SİSTEM

Sel, Kaan

Yüksek Lisans, Elektrik ve Elektronik Mühendisliği Bölümü
Tez Yöneticisi: Prof. Dr. Haluk Külâh

Temmuz 2018, 73 sayfa

Dielektroforez (DEF), kanserin erken teşhisinde kullanılabilir umut verici bir hücre manipülasyon yaklaşımı sunmaktadır. Yüzey antijenlerine dayanan ve düşük seçiciliğe sahip diğer manipülasyon metotlarından farklı olarak, DEF sistemler etiketsiz, düşük maliyetli ve kolayca uygulanabilir bir hücre karakterizasyonu ve ayrıştırmasını mümkün kılar. Ancak, günümüzde kullanılan DEF tabanlı sistemlerin ayrıştırma başarısı kanserin erken teşhisi için gerekli tıbbi şartları karşılamaktan uzaktır. Mevcut DEF sistemlerinin verimliliğini arttırmak için, optimum çalışma koşullarını elde etmek önemlidir. Bu tezin ana amacı, farklı çalışma koşullarında kanser hücrelerinin dielektroforetik karakterizasyonunu, herhangi bir dielektrik hücre değerini kullanmadan, otonom bir şekilde gerçekleştirebilmektir.

Tez kapsamında sunulan sistemin nihai versiyonu, CMOS görüntü sensörü, portatif sinyal üretici ve mikro-akışkan DEF cihazını birleştirir. Sistem, geniş bir frekans bandında (30 kHz ile 50 MHz arası) hücrelerin DEF spektrum analizini mümkün kılar. Mikro-akışkan DEF cihazı, aktif analiz bölgesi içerisinde izomotif elektrik alanı oluşturma yeteneğine sahip, özel tasarım elektrot yapıları içermektedir. Bu sayede, DEF kuvveti etkisi altındaki hücre hareketi doğrudan hücrenin dielektroforetik davranışı ile ilişkilendirilebilir.

Testlerde elde edilen kayıtların işlenmesi, otomatik hücre takip algoritması kullanan özel geliştirilmiş MATLAB GUI üzerinde ve akıllı telefona bağlanarak kullanılabilen Android yazılımında yapılabilmektedir.

Bu tez kapsamında sunulan DEF karakterizasyon cihazı ile, farklı koşullar hücre ayırıştırması için gerekli optimum koşulları bulmak amacı için, otonom ve titiz bir şekilde test edilebilir. Sistemin performans ve hassasiyet ölçümleri MCF-7 (insan meme adenokarsinomu) ve K562 (insan kronik miyeloid lösemi) hücreleri üzerinde yapılmıştır. Elde edilen sonuçlar, literatürde bu iki hücre grubu hakkında yer alan DEF spektrum çalışmaları ile uyum göstermektedir.

Anahtar Sözcükler: Dielektroforez (DEF), dielektrik hücre karakterizasyonu, tekil hücre analizi, BioMEMS, izomotif elektrik-alan

To my mother, father, and sister

ACKNOWLEDGMENTS

I would first like to express my sincere gratitude to my advisor Prof. Dr. Haluk Klah for his endless support towards realizing my goal of becoming an innovative and capable research and development engineer. Without his limitless wisdom, sincere understanding and extensive guidance, I could not successfully accomplish my academic journey.

I would also like to thank to my partner Mahmut Kamil Aslan for his strong motivation and solid faith in our challenging studies. I would like to thank to my dearest friends Metin Dndar zkan, Volkan Mehmet İřlek, Onur Memiođlu, Miraç Eren Aydođan, Deniz Sargun and Berker Pekz for their unwavering support and encouragement which worth more than I can express on paper. I would also like to thank to Yađmur Demircan for sharing her immense knowledge with me, to Taylan Berkin Tral, Levent Abat, Adem Saraç, Orhan Akar and other METU MEMS researchers, for their guidance and support in my thesis studies. They have never hesitated to offer a hand whenever I needed.

BioMEMS research group has provided me unique abilities to improve myself, but most importantly it allowed me to be a part of a great family. For this reason and for many more, I would like to thank to Metin Dndar zkan, Salar Chamanian, Hasan Uluřan, Eren Aydın, Bedirhan İlik, Furkan Gkçe, Didem Çetin, Begm řen Dođan, Yađmur Demircan, Aziz Koyuncuođlu, Taylan Berkin Tral, Parinaz Ahsrafi zkayar, Ali Can Atik, Grhan zkayar, Ceren zcan Ateř, Ahmet Efe, Alper Kaan Soydan, Berat Yksel, Berkay Çiftçi (special thanks), and Andaç Yiđit.

It takes a multidisciplinary background, a diverse skill set and of course hard work in order to design and implement a state-of-the-art system. However, it would have been impossible, without the support from the ones who were always there for me. In this manner, I would like express my very profound gratitude to my parents Belgin and Tayfun Sel and my sister Ece for keeping their unfailing support and continuous encouragement all the time.

During this study, I gratefully acknowledge The Scientific and Technological Research Council of Turkey (TUBITAK) for the financial support through project 213E024 and scholarship support, and Ministry of Development, the Republic of Turkey through project BAP-2016K121290 for the financial support.

TABLE OF CONTENTS

ABSTRACT	v
ÖZ.....	vii
DEDICATION	ix
ACKNOWLEDGMENTS.....	x
TABLE OF CONTENTS	xii
LIST OF TABLES	xv
LIST OF FIGURES.....	xvi
1 INTRODUCTION.....	1
1.1 Particle manipulation techniques through BioMEMS applications	2
1.1.1 Optical Manipulation.....	2
1.1.2 Magnetic Manipulation	4
1.1.3 Mechanical Manipulation.....	5
1.1.4 Dielectrophoretic Manipulation	5
1.2 Research Objectives and Thesis Organization	6
2 DIELECTROPHORETIC CELL CHARACTERIZATION.....	9
2.1 Theory of Dielectrophoresis	9
2.2 Dielectrophoretic Cell Sorting.....	12
2.3 Dielectrophoretic Cell Characterization	13
2.4 Cell Modelling.....	14
2.4.1 Electrical Circuit Equivalent for Biological Cells.....	15
2.4.2 Parametric Simulation of Dielectric Model for $Re(fcm)$ Calculation	16

2.4.3	Dielectric Modelling of MCF-7 (Human Breast Adenocarcinoma) & K562 (Human Chronic Myeloid Leukemia) Cells.....	18
2.5	Literature Survey on Dielectophoretic Spectra of K562 and MCF-7 Cells	19
3	DESIGN, SIMULATION AND FABRICATION OF THE DIELECTROPHOTRETIC CHARACTERIZATION DEVICE	25
3.1	Electrode Configuration and Device Design.....	25
3.1.1	V-shaped planar electrode.....	25
3.1.2	Electrode Configuration Evolution for Isomotive Electric Field Generation	29
3.2	Finalized Electrode Configuration and the Microchannel Design	30
3.3	Analysis Methodology	34
3.4	Electric Field Fitting with MATLAB.....	35
3.5	Fabrication.....	37
4	EXPERIMENTATION, RESULTS AND DISCUSSION OF THE DIELECTROPHORETIC CHARACTERIZATION DEVICE.....	41
4.1	Testing.....	41
4.1.1	Sample Preparation	42
4.1.2	Microscopy Tests and MATLAB Post-Processing with MCF-7 cells.....	43
4.1.3	Cell Characteristics Deviation According to Cell Morphology	47
4.1.4	The Android Interface and Portable Lab-on-a-chip (LOC) System on K562 cells	48
4.2	Results	52
4.2.1	Experimental Verification.....	52
4.2.2	Test Results on MCF-7 cells.....	54
4.2.3	Test Results on K562 cells.....	54

4.3 Discussion.....56

 4.3.1 Experimental Drawbacks and Applied Solutions.....56

5 CONCLUSION AND FUTURE WORK.....61

REFERENCES63

LIST OF TABLES

Table 1 The average dielectric values of MCF-7 and K562 cells that are available in the literature.	18
Table 2 Cell characterization results reported in the literature on K562	21
Table 3 Cell characterization results reported in the literature on MCF-7	23

LIST OF FIGURES

Figure 1.1 Illustration of the main optical cell manipulation techniques [87].	3
Figure 1.2 Illustration of magnetic cell manipulation techniques and their possible use cases [87].	4
Figure 2.1 DEP spectra of two particles A and B. At the frequency point denoted by f_{sep} , particle A experiences a positive DEP force, while particle B is experiencing negative DEP force. Therefore at this frequency, these two particles can be separated [88].	12
Figure 2.2 Electrical illustration of cell membranes and cell nucleus. Image by Bryan Christie Design.	15
Figure 2.3 Simulation results of single shell cell modelling. (a) The comparison of DEP responses between two particles having radiuses R1 and R2, where identical otherwise. (b) Effect of medium conductivities were shown, where σ_{med1} is larger than σ_{med2} . (c) Cell membrane conductivity effect is shown (d) Cell cytoplasmic conductivity effect is shown.	17
Figure 2.4 DEP spectrum simulation results of MCF-7 cells at the medium conductivity, $\sigma_{med} = 2.5$ mS/m.	19
Figure 2.5 DEP spectrum simulation results of K562 cells at the medium conductivity, $\sigma_{med} = 2.5$ mS/m.	20
Figure 3.1 The electrode and channel configuration of the initially fabricated DEP characterization devices in BioMEMS research group [79].	26
Figure 3.2 Electric field simulation results of the overall geometry, where $\nabla E_{rmsr}, \omega^2$ results are illustrated. It is observed that the force field is not uniform.	27
Figure 3.3 COMSOL modelling and material definitions.	27
Figure 3.4 Electric-field simulation results at different heights. It is seen that z-axis has an effect on the field direction and magnitude near the electrodes.	28

Figure 3.5 Electric-field simulation results of the analysis region (400 μm x 400 μm) box. Only half of the box is shown due to symmetry.	28
Figure 3.6 Electric-field simulation results of circular vs. vertical electrode configuration	30
Figure 3.7 Electric-field simulation of concave electrodes opposing each other.	31
Figure 3.8 Electric field simulations of concave and convex electrodes facing each other with different radiuses. The radius values were swept and the results are illustrated in the figure.	32
Figure 3.9 The fabricated device and device dimensions	32
Figure 3.10 ∇E^2 (force field) simulation and electric field fitting results. (a) The isomorphic behavior of the electric field for the active monitoring region (on x-y plane at $z = 10\mu\text{m}$, half of the channel length). (b) Schematic of the microfluidic device. (c) Distribution of the force field in x-z plane (at $y = 0$).	33
Figure 3.11 Triangular surface meshing with maximum element size set at 3 μm and other element size parameters set at their default values (calibrated for General physics, extremely fine meshing) was swept to the whole body with Quadrilateral face meshing method having 40 distribution elements in COMSOL Multiphysics for electrical simulations.	35
Figure 3.12 Square fitting of triangular mesh with 1 μm x 1 μm dimensions. Magnitude of the x-component of the force field extracted from COMSOL simulations fitted in MATLAB platform in x-y domain is shown on z-axis of the illustration.	36
Figure 3.13 Fabrication flow of the DEP characterization device.	37
Figure 3.14 The fabrication masks for PR patterning.	38
Figure 4.1 The microscopy test setup. (a) Overall test setup including Ratio imaging inverted research microscope at 5x zoom, microfluidic flow control system, fluorescence light source and microfluidic DEP chip (b) Signal generator. 10 V_{p-p} AC signal at 15 different frequencies ranging between 30 kHz and 50 MHz was applied to electrodes with 180° phase difference in between (c) Microfluidic DEP chip.	44

Figure 4.2 Video processing with MATLAB. (a) MATLAB GUI for investigation of recorded cell motions. The procedure is as follows; i. Video selection. ii. Video rotation (if necessary) for consistency in x-y domain definitions. iii. Selection of concave electrode tips for automatic tilting and pixel to metric calculations. After clicking on ‘calibrate’ button the previously dedicated cell tracking area appears. iv. User dedicated selection of active cell monitoring area. v. Start of frame by frame video processing for cell tracking. vi. Selected video name. vii. Selected calibration point coordinates.45

Figure 4.3 Previously dedicated cell tracking area appears after calibration is completed. Green square corresponds to the user selection for active monitoring area, where program automatically zooms to the new area. Video is read and sampled into frames with 30 fps rate. Then images were converted into greyscale followed by adaptive histogram equalization, 2-D median filtering, and binarization by thresholding steps.....46

Figure 4.4 Correlation between the test results of K562 cell line. Area inside the blue ellipses shows that the majority of the cells in the range from 0.4 to 0.6. Red line is drawn at 0.5, showing the average.47

Figure 4.5 Target cells used in DEP spectrum investigation. i. Cells exhibit the average DEP characteristics. ii. cells show a scattered response to the DEP field.....48

Figure 4.6 Signal generator circuit including ATmega microcontroller, 6009 DC to DC boost circuitry and AD9850 waveform generator IC. Also, an adjustable voltage amplifier stage was implemented. Sinusoidal voltages with 180° phase difference was generated by AD9850 IC. The microcontroller was programmed via Arduino board to control the frequency of the generated sinusoidal voltage between 0 and 50 MHz. Generated signals were amplified to 20 Vp-p employing voltage amplifier with single supply OPAMP configuration. DC supply voltage of the USB interface (5V) was boosted using XL 6009 IC to bias the OPAMPs.50

Figure 4.7 LOC system. (a) CMOS image sensor and DEP device placed with-in 3-D printed holder connected to a smartphone via micro-USB connection. Portable signal generator circuit mounted in 3-D printed holder to generate two sinusoidal signals with 180° phase difference at desired frequency. (b) Custom-developed Android software. It is

used to communicate with CMOS image sensor and conduct frame by frame investigation.51

Figure 4.8 Processed image at $t=0$ and $t = 10$ s, where cell is attracted towards the concave electrode under the influence of positive DEP force field.51

Figure 4.9 Comparison of cell velocity and generated electric field gradient at cell's position. As expected, cell velocity is directly related to the electric field gradient curve, hence $Re(fcm)$ value becomes position and time independent.53

Figure 4.10 Snapshots corresponding to the experiment on MCF-7 cells at 1 MHz, taken at different time intervals. It is seen that under the influence of a DEP force MCF-7 cells start to move towards the convex electrode.54

Figure 4.11 DEP Spectrum of MCF7 cells. Cross-over frequencies were found as 107 kHz and 35.4 MHz. Between these frequencies, cells are attracted to denser electric-field regions (positive DEP).55

Figure 4.12 DEP spectrum results of K562 Myelogenous leukemia cell line. The cross-over frequencies appeared at 200 kHz and 39.8 MHz. In addition, cells experienced lower magnitude of negative DEP force compared to positive DEP force.55

Figure 4.13 Microscopy snapshot of the microchannel with two different solutions at two different times. (a) Image corresponding to continuous flow where dead cells dominate the flow and disable successful tests. (b) A pure cell solution with residue-free environment. Notice that the channel only contains live cells.58

Figure 4.14 Cell count of K562 cells prior to the testing. 96% of the cells are alive. This is a prerequisite for testing to start.58

Figure 4.15 Reservoir plantation to the channel inlet.59

CHAPTER 1

INTRODUCTION

According to the report published by World Health Organization (WHO) on 2018, the second leading cause of mortality is cancer, where 1 of 6 of the deaths was due to cancer in 2015, globally [1]. The psychological and economic burden is also increasing with the increase in the number of reported cancer diagnosis [2]. There are many studies and research that focuses not only on preventing this deadly disease but also on successful treatment of it. In most of the cases detection and therefore treatment after symptom onset, increases the morbidity, mortality rate and cost of treatment. On the other hand, early diagnosis before the symptom onsets proved itself to be a key point in successful treatment. The survival rate of patients are reported to be increased from 5% to more than 90%, when compared to cancer detection at most advanced stages [3], [4].

Many methods were tested and improved in the effort of early cancer detection for decades. Tumor markers, being consulted for decades in oncology enable cancer screening up to a certain level [5], [6]. These biomarkers associate to cancer, and can be found in urine, blood, or in other body tissues. However, these biomarkers demonstrate poor accuracy in addition they require regular screening of every possible future cancer victim. It is not feasible, especially as WHO reported that the 70% of deaths due to cancer occurred in countries with low- and middle-incomes. In addition, in the same report only 26% of countries with low-income have public available cancer treatment opportunities. Therefore, low-cost methods take more of the attention with the increase in the technological capabilities.

Our capabilities with current technology improved way beyond our expectations back in last few decades. In addition, systems start to shrink in size, creating new opportunities for researchers and engineers enabling micro- and nano-scale device designs for various purposes. As semiconductor devices along with integrated systems and circuits started to push the limits of physical laws, systems-on-a-chip (SoC) applications called attention of the designers. These applications include biomedical device designs that aim to bring innovative and systematic solutions to medical problems. Within the extensive work and effort on micro-electro-mechanical system (MEMS) design and development, biomedical or biological systems adapt into MEMS forming the field of BioMEMS [7], [8]. BioMEMS has now variety of biomedical applications that find revolutionary solutions to existing problems [9]. These applications range from surface modification, drug delivery, bio-implementable systems to diagnostic based systems. Unlike the conventional diagnosis systems, the advantage of bringing MEMS approach is to develop lab-on-a-chip (LOC) systems in order obtain a disposable, low-cost manufacturing ability, as well as enabling single cell level analysis. With the utilization of MEMS tools, certain particle manipulation techniques were developed. These techniques can be modified in a certain way to detect cancer cells at early stage.

1.1 Particle manipulation techniques through BioMEMS applications

Different approaches were constructed in order to manipulate biological particles instead of just monitoring with high resolution microscopes as the emerging of microfluidics in 1980s. Through microfluidics precise control on the fluid dynamics were gained. Therefore, the environment at sub-millimeter scale for particle manipulation could be set. The main driving thing in particle manipulation is to generate a force variable in a form of optical, magnetic, mechanical or electrical forces. Hence, cell trapping, sorting, separation as well as characterization became possible in single-cell level.

1.1.1 Optical Manipulation

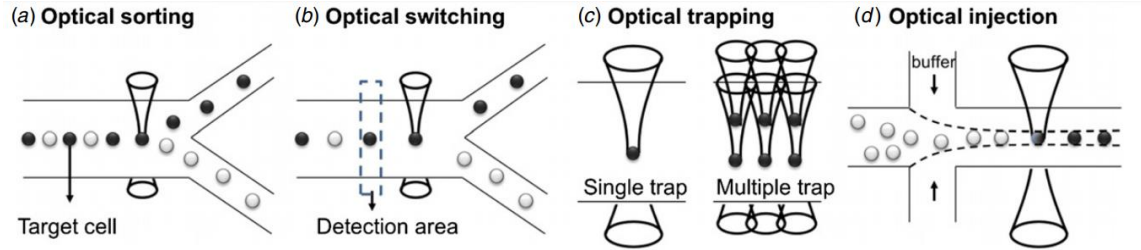


Figure 1.1 Illustration of the main optical cell manipulation techniques [87].

The optical force is generally generated by a focused laser beam on the particle surface through an objective with high numerical aperture of usually a microscope [10], [11]. It is either in the form of pulling force or scattering force on target particle by using the differences between a gradient optical forces. When the pulling force can overcome the scattering force the particle is optically trapped. Optical manipulation techniques were illustrated in Figure 1.1.

Eriksson et al. studied targeting yeast cells using the differences in the cell size and the refractive index, in order to position cells by optical trapping [12]. Although the technique was easy to apply on single-cell level, the throughput was low. A similar study was conducted by Dochow et al. on human blood cells this time, using the differences in the cell sizes, however similar to before, the throughput was reported very low [13]. A high throughput cell sorting was reported on mammalian cells by Wang et al. [14]. However, they used fluorescence markers in order to initiate optical switching, increasing the cost and introducing damage on cell structure.

Optical manipulation techniques are accounted to several limitations and drawbacks. First of all, in order to obtain high throughput, samples should be highly purified and optically homogeneity preparations should be conducted. Secondly optical trapping suffers from selectivity problems, where any dielectric particle may experience the force and get trapped. Therefore, the purity of the solution should be extremely exercised. In addition, the requirement of having a high light intensity to trap particles successfully causes damage on the cell and introduce new dynamics to the analysis.

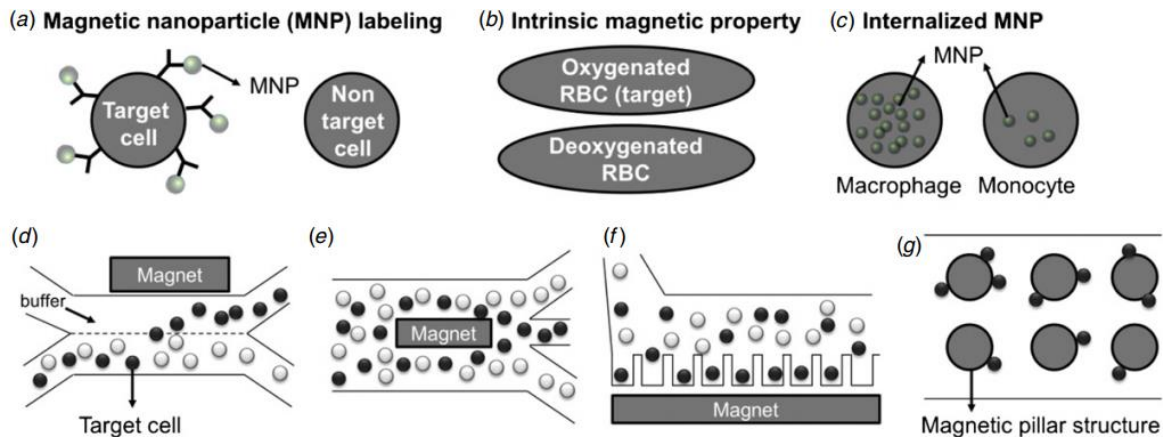


Figure 1.2 Illustration of magnetic cell manipulation techniques and their possible use cases [87]

1.1.2 Magnetic Manipulation

Magnetic manipulation technique can be employed on either intrinsic or extrinsic cell properties. A typical example in the utilization of intrinsic properties is generating a magnetic force based on hemoglobin (containing iron element) in erythrocytes [15]. In some applications, magnetic nanoparticles are used to provide a difference in the magnetic properties to the target particles to create different magnetic forces for sorting. Several magnetic manipulation examples were illustrated in Figure 1.2.

There are high-throughput cell separation results reported in the literature that uses magnetic bead labeling. Shih et al. separated bacterial cells by the use of a high gradient magnetic field [16], Kang et al. isolated rare cells by magnetically collecting within the chamber [17], Hoshino et al. did a cell analysis on cancer cells by monitoring self-assembled magnetic bead patterns [18], where all of these studies initially tagged the cells with magnetic beads to generate magnetophoretic force. Another study reported a high-throughput magnetophoretic separation of human blood cells using interior cell magnetic properties [19]. All common drawbacks in these systems was the difficulty of single-cell level analysis. In addition, most magnetic manipulation systems require the use of magnetic beads, eliminating label-free operation. One another major drawback with magnetic manipulation is that the magnet configuration is robust hence it limits the

manipulation ability. Sensitivity is also low but can be improved but it still requires extensive effort [20].

1.1.3 Mechanical Manipulation

Mechanical manipulation technique was developed mainly with the development of hydrodynamic control in the microfluidic device. The simplest approach to manipulate target cell and separate it from the environment is to design a gate inside the microchannel with the size as small as the cell can pass. Although it seems easy to apply, this approach suffers from clogging and possible residues inside the channel.

High-throughput in size based separation can be achieved when the size difference between target and adjacent cells are significant. There are studies that successfully separates human blood cells using this technique, where the microfluidic flow was used to drive cells to the gaps [21]–[23]. However, mechanical manipulation lacks the ability to differentiate cells having similar physiologies, therefore the throughput is low in cancer cell analysis [24].

1.1.4 Dielectrophoretic Manipulation

The aforementioned manipulation techniques either lack the ability of label-free operation or perform separation with poor efficiency or low selectivity. In addition, the introduction of surface antigens and tags have several side effects on the target cells, increasing the overall costs [25]–[28]. On the other hand, dielectrophoresis (DEP) provides cost-effective, simply-implementable and label-free operation and can be utilized for cell manipulation [29]–[32]. The DEP phenomenon is based on the manipulation of particles depending on their unique dielectric properties (i.e. cytoplasmic and membrane conductivity and permittivity values) [33]. There are several reports in the literature about successful separation and manipulation of biological particles including bacterial cells [34]–[36], viruses [37], tumor cells [38]–[40], and stem cells [41], with DEP. However, medical applications for early cancer detection demand a work with very low concentrations of target cells (~ 1-3 cell/ml) in blood suspension [42].

In order to operate under very low rare cell concentrations, the constructed DEP separation systems should be accurately optimized. In the ideal case, with the exact knowledge of dielectric properties (permittivity and conductivity) of target cells, it is possible to calculate the DEP force generated inside a known medium and obtain the separation efficiency. However, due to the dynamic behaviour of biological organisms, cell physiology (membrane and cytoplasmic properties) varies in time [43], [44]. Hence, an accurate cell characterization system should be established as the initial and indispensable step of dielectric cell manipulation applications.

Dielectrophoretic cell characterization systems investigate cell behaviour under a non-uniform electric field at different frequencies to obtain DEP spectra of the cells. By obtaining DEP spectra of target cells that spans a wide frequency band, the separation frequency of the target cells from the adjacent cell suspension can be obtained. Therefore, the separation efficiency of DEP devices increases. Usage of a DEP characterization system to increase cell separation efficiency through DEP has previously been reported in other studies [38], [45]. However, a strong connection between theory, detailed simulations, and design parameters of the characterization system are missing in the literature. This thesis study proposes a dielectrophoretic characterization system that uses experimental data to assess DEP spectra of cancer cells without ascertaining cell dielectric properties.

1.2 Research Objectives and Thesis Organization

The primary research objective of this thesis is to develop a microfluidic system for dielectric characterization of cancer cells. Hence, the system can be used to optimize the operating conditions of separation devices that rely on DEP in order to meet the medical requirements.

To achieve this objective, following studies are aimed:

- Development of an analysis methodology backed-up with strong theoretical explanations, in order to characterize particles without ascertaining dielectric properties of cells.
- Design of a microchannel with unique electrode structures that generates non-uniform but isomotive electric-field in order to simplify complex mathematical force equations.
- Modelling of the design parameters and conducting electric-field simulations of the 3-dimensional constructed geometry with COMSOL Multiphysics software.
- Development of the fabrication flow and masking layers, and fabrication of the microchips.
- Creating an unbiased and rigorous testing environment, testing the DEP characterization devices with available cancer cell lines.
- Post-processing the test results, verifying the constructed analysis methodology through experimental feedback, and obtain dielectrophoretic spectra of cancer cells.

This thesis has been organized in four chapters as follows:

Chapter 2 introduces the DEP theory and DEP characterization concept including results and discussion of the dielectrophoretic modelling of the cancer cells that were studied in this thesis. At the end of the chapter, an extensive literature survey is presented on dielectrophoretic characterization of MCF-7 and K562 cells.

Chapter 3 is dedicated to introduce the proposed DEP characterization devices in detail. The chapter contains sections about the design of the electrodes for isomotive electric field generation, the construction of an analysis model and MEMS fabrication.

Chapter 4 gives two different measurement setups including different analysis methods. The testing procedure as well as results are also shared in this chapter. In addition, the results section contains experimental verification of the analysis model.

Lastly, chapter 5 presents the thesis conclusion and possible future upgrades that can be applied to the presented system to be able to use the system for various applications. In addition, minor modification recommendations were shared.

CHAPTER 2

DIELECTROPHORETIC CELL CHARACTERIZATION

2.1 Theory of Dielectrophoresis

Dielectrophoresis (DEP) was firstly defined by Herbert Pohl to describe the translational motion of neutral matter caused by polarization effects in a non-uniform electric field [46]. According to this phenomenon, DEP occurs when a polarizable particle is suspended in a non-uniform electric field. Under this position dependent field, the force generated through the difference in the dielectric properties of particles and medium is called as dielectrophoretic (DEP) force. Time averaged version of the DEP force is expressed in Equation (1) for spherical particles, which applies to living cells [37].

$$\langle \vec{F}_{DEP} \rangle = 2\pi\epsilon_m r^3 \text{Re}(f_{cm}) \nabla |\vec{E}_{rms}(r, \omega)|^2 \quad (1)$$

Here, \vec{F}_{DEP} refers to the DEP force, ϵ_m is the medium permittivity, r is the radius, f_{cm} corresponds to Clausius-Mossotti relation, which depends on the frequency of the applied electric field, $\vec{E}_{rms}(r, \omega)$, with the following relation [47],

$$f_{cm} = \frac{\epsilon_p^* - \epsilon_m^*}{\epsilon_p^* + 2\epsilon_m^*} \quad (2)$$

Remark that, in the Clausius-Mossotti relation, permittivity values are complex, meaning that they are frequency dependent with the below relation.

$$\varepsilon^* = \varepsilon + j \frac{\sigma}{\omega} \quad (3)$$

Here, σ refers to the conductivity, ω is the angular frequency of the applied voltage, and j is equal to $\sqrt{-1}$. By combining complex permittivity expression with Clausius-Mossotti relation and regrouping the complex and real components,

$$f_{cm} = \frac{(\varepsilon_p - \varepsilon_m) + j\left(\frac{\sigma_p}{\omega} - \frac{\sigma_m}{\omega}\right)}{(\varepsilon_p + 2\varepsilon_m) + j\left(\frac{\sigma_p}{\omega} + 2\frac{\sigma_m}{\omega}\right)} \quad (4)$$

Only the real part of Equation (4) appears in the force relation and it is given by,

$$Re(f_{cm}) = \frac{(\sigma_p - \sigma_m)(\sigma_p + 2\sigma_m) + \omega^2(\varepsilon_p - \varepsilon_m)(\varepsilon_p + 2\varepsilon_m)}{(\sigma_p + 2\sigma_m)^2 + \omega^2(\varepsilon_p + 2\varepsilon_m)^2} \quad (5)$$

Equation (5) implies that for low frequencies (roughly below 10 MHz) the conductivities of the particle and medium are dominant, and $Re(f_{cm})$ becomes [48],

$$Re(f_{cm}) = \frac{\sigma_p - \sigma_m}{\sigma_p + 2\sigma_m} \quad (6)$$

At higher frequencies $Re(f_{cm})$ becomes permittivity dependent as shown in Equation (7).

$$Re(f_{cm}) = \frac{\varepsilon_p - \varepsilon_m}{\varepsilon_p + 2\varepsilon_m} \quad (7)$$

The amount of the generated DEP force depends on the rate of change in the applied electric field. It is governed by the gradient expression of the root-mean-square value of the applied AC electric field. Electric field in 3-dimensional space is written as,

$$\vec{E}(r, \omega) = E_x \hat{x} + E_y \hat{y} + E_z \hat{z} \quad (8)$$

Therefore, the force field, $\nabla |\vec{E}_{rms}(r, \omega)|^2$, becomes,

$$\begin{aligned} & \nabla |\vec{E}_{rms}(r, \omega)|^2 \\ &= \left(E_x \frac{\partial E_x}{\partial x} + E_y \frac{\partial E_y}{\partial x} + E_z \frac{\partial E_z}{\partial x} \right) \hat{x} \\ &+ \left(E_x \frac{\partial E_x}{\partial y} + E_y \frac{\partial E_y}{\partial y} + E_z \frac{\partial E_z}{\partial y} \right) \hat{y} \\ &+ \left(E_x \frac{\partial E_x}{\partial z} + E_y \frac{\partial E_y}{\partial z} + E_z \frac{\partial E_z}{\partial z} \right) \hat{z} \end{aligned} \quad (9)$$

Notice that this expression is strongly position dependent. Therefore, it causes complexity in the precise integration of the force field throughout the particle's trajectory.

Frequency of the applied voltage affects the magnitude of generated DEP force, in addition to determining the direction of the motion. If the particle is attracted to a denser electric field at a certain frequency, a positive DEP force is generated. On the other hand, if the particle moves in favour of a sparse electric field flux, a negative DEP force is produced. There is a special case, in which the particle feels no force and the corresponding frequency at this point is called cross-over frequency [33].

It is critical to define the cross-over frequencies, as well as the negative and the positive DEP regions of the target and adjacent cells in order to have a properly working

dielectrophoretic cell separation system. In order to understand this it is essential to understand the operation of a DEP based separation system.

2.2 Dielectrophoretic Cell Sorting

DEP based cell sorting (i.e. separation) is a system that aims to identify target cells from its environment using the differences in the dielectrophoretic properties. This is possible by finding an optimum operating point in which target cells and adjacent cells (cancer cells in this case are the target cells and blood cells are the adjacent cells) experience different forces either in magnitude or in direction or in both magnitude and direction. For this reason, if the DEP spectra of both cell groups was obtained, a frequency point in which each cell group experience different DEP forces could be found as illustrated in Figure 2.1.

Recent studies that uses DEP to assess cancer in clinical samples report separation efficiency up to a limited level [49]–[51] still far from meeting the medical requirements.

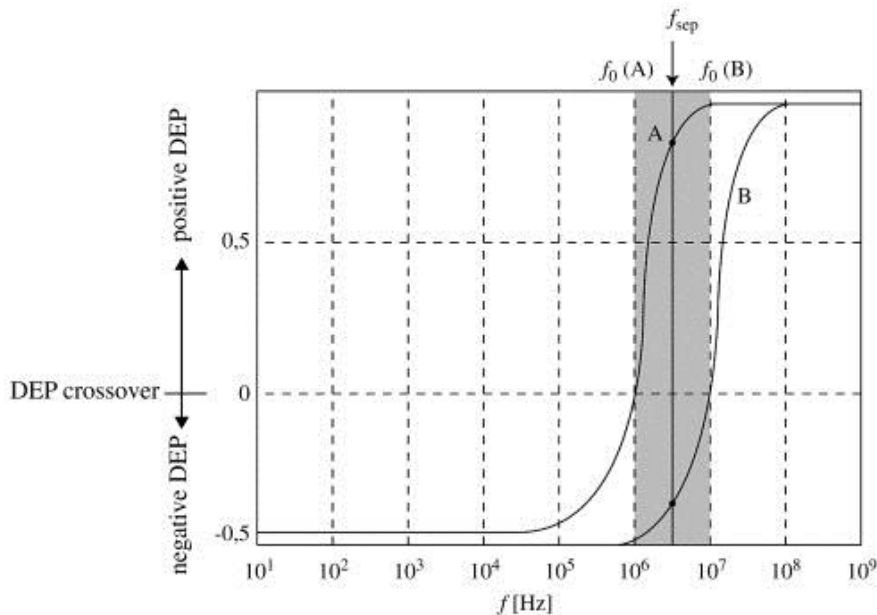


Figure 2.1 DEP spectra of two particles A and B. At the frequency point denoted by f_{sep} , particle A experiences a positive DEP force, while particle B is experiencing negative DEP force. Therefore at this frequency, these two particles can be separated [88].

As discussed before, this is because the dynamic behaviour of cell structure. For this reason, current DEP characterization methods that rely on cell models and assumptions should be improved with more solid and experimental characterization methods.

2.3 Dielectrophoretic Cell Characterization

Dielectrophoretic cell characterization systems investigate cell behavior under a non-uniform electric field at different frequencies to obtain DEP spectra of the cells (i.e. $Re(f_{cm})$ and frequency relation). The Clausius-Mossotti factor, $Re(f_{cm})$, is dependent on frequency of the applied field, dielectric properties of the suspending DEP medium and cells. By obtaining DEP spectra of two different cell groups under identical experimental conditions, in a wide frequency band, the optimum frequency can be obtained to separate these two groups from each other. Therefore, the cell separation throughput is improved. Usage of a DEP characterization system to increase cell separation efficiency through DEP has also previously been reported in other studies [38], [45], [52]–[54]. However, a strong connection between theory, detailed simulations, and design parameters of the characterization system are missing in the literature.

In order to obtain $Re(f_{cm})$ of target cells by investigating their motion under the influence of DEP field a certain analysis methodology was constructed. Initially, cells were assumed to be point-particles. To proceed, the following assumptions were made [55],

- No thermal effect on flow field and velocity
- Cell and channel walls do not react with medium fluid
- Rotation of the particle does not affect translational motion
- Reynold's number satisfies the laminar flow condition
- No electrostatic interaction between the particles

At the creeping flow limit, known as Stoke's law, drag force is [56],

$$\vec{F}_{drag} = 6\pi\mu r(\vec{u}_m - \vec{u}_p) \quad (10)$$

Here, $R, \mu, \vec{u}_m, \vec{u}_p$ and \vec{u}_0 are particle radius, viscosity of the suspending medium, medium fluid velocity, instantaneous particle velocity and initial particle velocity. By going through Newton's second law, following relation was obtained,

$$m_p \frac{d\vec{u}_p}{dt} = -6\pi\mu r(\vec{u}_m - \vec{u}_p) + \vec{F}_{DEP} \quad (11)$$

In order to apply Stoke's law, the particle should be several diameters away from other particles and the walls of the system and the flow should be laminar. Therefore, only a single cell should be examined, in order to eliminate cell to cell interactions. Two different analysis methods were constructed and tested on two different generation DEP characterization devices. The details of the analysis methodology is discussed in the next chapter.

2.4 Cell Modelling

DEP is a popular cell manipulation technique, and DEP theory is extensively been worked in numerous of studies as discussed previously. With the increase in the number of researches that had been conducted on DEP, electrical characterization of the cells also occupied some part of the literature. In order to understand the parameters let us go back to the components of Equation (1). Remark that only the real part of Clausius-Mossotti relation (f_{cm}), is dependent on cell properties as it is expressed in Equation (1). The difference in the complex permittivity values of the cell and the suspending DEP medium generates a non-zero difference, which determines the relative magnitude and direction of the generated DEP force. This implies that, if the complex permittivity of the target cell or the cell group is known, it is possible to calculate magnitude and direction of the generated DEP force, hence to differentiate cancer cells from regular blood cells in clinical

samples. This motivation led researchers to electrically model cell structure. This section discusses the representation of cell interior and structures using electrical based analogy, and modelling results of MCF-7 Human Breast Adenocarcinoma cells and K562 Human Chronic Myeloid Leukemia cells.

2.4.1 *Electrical Circuit Equivalent for Biological Cells*

A typical cell is composed of a cell cytoplasm and a cellular membrane. The cellular membrane controls the ionic balances and density flows by being semi-permeable. The cellular membrane is composed of lipids, proteins and other complex structures, where they exhibit a molecular structure known as “fluid mosaic model” [57]–[60]. The membrane as well as the cytoplasm (cytosol) can be represented as series and parallel connections of resistors and capacitors. Where organelles, nucleuses, and cell membranes can be represented as capacitive elements and the conductive cytoplasmic liquid suspending the structure can be modelled as resistors as illustrated in Figure 2.2.

In this representation, nucleated cell is assumed to be a homogeneous sphere with effective complex permittivity, ϵ_p^* [40], [53], [61]–[63]. In order to be able to use the modelling

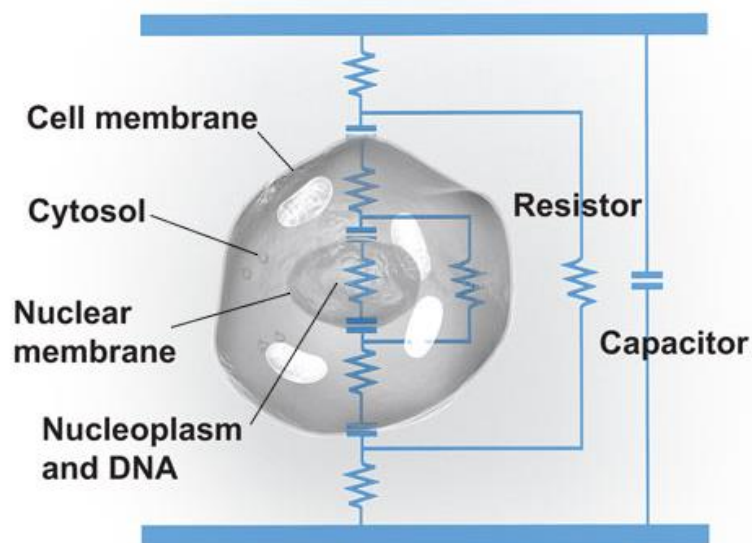


Figure 2.2 Electrical illustration of cell membranes and cell nucleus. Image by Bryan Christie Design.

data in Clausius-Mossotti factor calculation it is important to formulate the effective complex permittivity based on cytoplasmic and membrane conductivities and cell dimensions and understand the permittivity, conductivity relation with capacitance and resistance.

The conductivity and resistivity relations are given by,

$$C = \varepsilon \frac{\pi r^2}{d} \quad (12)$$

$$R = \frac{2\pi r}{\sigma \pi r^2} \quad (13)$$

R and C corresponds to resistance and capacitance respectively, r as introduced before is the cell radius and d is the thickness of the cell membrane. According to single shell model complex permittivity value of the cell can be expressed as [64], [65],

$$\varepsilon_p^* = \varepsilon_{mem}^* \left[\frac{(r/(r-d))^3 + 2[(\varepsilon_{cyt}^* - \varepsilon_{mem}^*)/(\varepsilon_{cyt}^* + 2\varepsilon_{memb}^*)]}{(r/(r-d))^3 - [(\varepsilon_{cyt}^* - \varepsilon_{mem}^*)/(\varepsilon_{cyt}^* + 2\varepsilon_{memb}^*)]} \right] \quad (14)$$

Here, ε_{mem}^* and ε_{cyt}^* represent the complex permittivity of the cell membrane and effective complex permittivity of cell interior (i.e. cytoplasm) respectively, and d is the membrane thickness. Using Equation (3, 12 – 14) it is possible to calculate overall effective cell permittivity. This can be used for modelling the dielectrophoretic behavior of the cell by calculating $Re(f_{cm})$ though inserting the corresponding DEP medium properties.

2.4.2 Parametric Simulation of Dielectric Model for $Re(f_{cm})$ Calculation

It is known that biological organisms, especially cancer cells exhibit dynamic behavior as discussed previously. Hence, cell modelling gives only a rough estimation about the dielectrophoretic spectra of cells. On the other hand, it is important to understand the effect of each parameter, such as cell radius, membrane and cytoplasmic conductivity as well as

suspending DEP medium conductivity on the DEP spectra. For this reason, before modelling MCF-7 and K562 cell lines, a parametric sweep of parameters in Equation (14) was conducted in MATLAB, where only one parameter is manipulated at a time. Figure 2.3 shows the simulation results that cover 4 different parameters. All other parameters were kept constant, except the one that is discussed at each section. Simulation parameters were taken from a previous report in the literature [63]. It is observed that, having R2 larger than R1, cells having larger radius have their first cross-over frequency earlier, however with a weaker negative DEP force experienced. In addition, an increase in medium conductivity shifts the first cross-over frequency to the higher frequency regions. Moreover, cells with higher membrane conductivity experience less negative DEP force at lower frequencies. According to this model cells having membrane conductivity more than $4 \mu\text{S}/\text{m}$ experience positive DEP force at all frequencies. On the other hand, cell cytoplasmic conductivity has an impact on the high frequency region unlike the other three

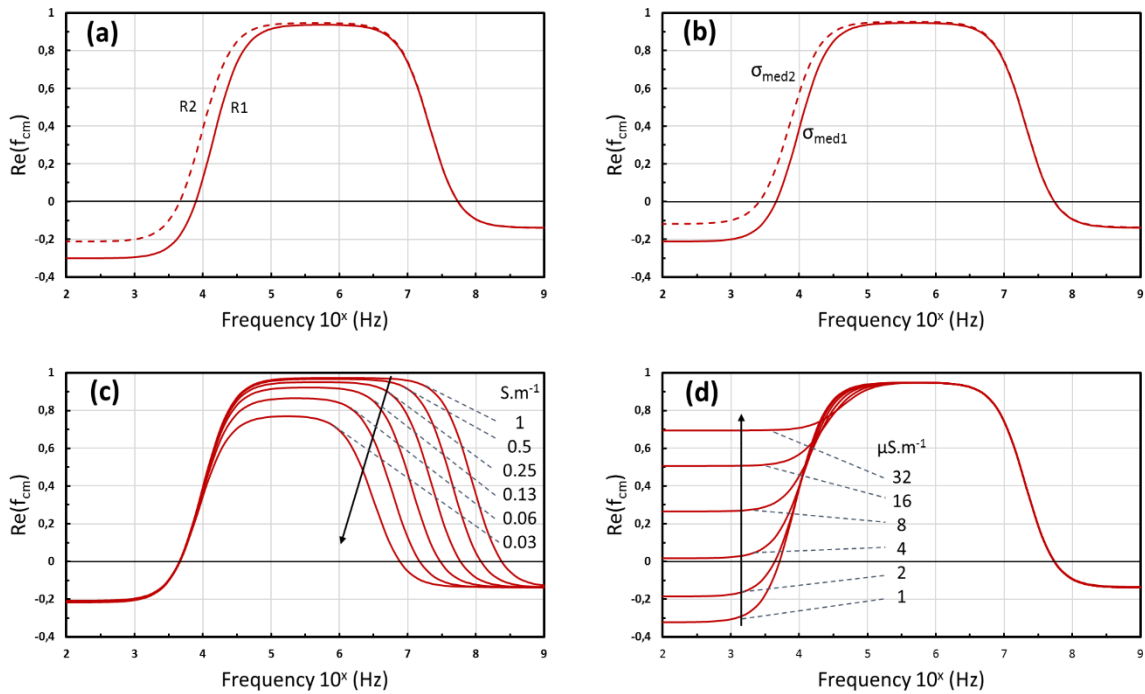


Figure 2.3 Simulation results of single shell cell modelling. (a) The comparison of DEP responses between two particles having radiuses R1 and R2, where identical otherwise. (b) Effect of medium conductivities were shown, where $\sigma_{\text{med}1}$ is larger than $\sigma_{\text{med}2}$. (c) Cell membrane conductivity effect is shown (d) Cell cytoplasmic conductivity effect is shown.

parameters discussed. It is shown that, with the increase in cytoplasm ion density, switching from positive DEP to negative DEP regions occurs in the further part of the frequency scale. One important realisation is that, none of the parameters, except cell cytoplasmic conductivity has an effect on high frequency behaviour and second cross-over frequency.

2.4.3 Dielectric Modelling of MCF-7 (Human Breast Adenocarcinoma) & K562 (Human Chronic Myeloid Leukemia) Cells

Two different cell groups, MCF-7 (Human Breast Adenocarcinoma) cells and K562 (Human Chronic Myeloid Leukemia) cells, were studied in the scope of this thesis because of the availability. In order to match the experimental characterization data with cell modelling, a literature survey was conducted to find the necessary values in Equation (14) for each cell group. Table 1 shows the average values of the dielectric parameters of these cell groups taken from the literature.

Notice that the value of the cytoplasmic permittivity for MCF-7 cell line is not available. Therefore, throughout the simulations 50 was taken for ϵ_{cyt} , based on a literature data that focuses on a similar cell line, MDA-MB231 [66].

Table 1 The average dielectric values of MCF-7 and K562 cells that are available in the literature.

Cell type	r (μm)	C _{mem} (mF/m ²)	σ_{cyt} (S/m)	ϵ_{cyt}	References
Average values of MCF-7	10.88	17.3	0.23	N/A	[67]–[69]
Average values of K562	8.70	9.20	0.25	40	[52], [70], [71]

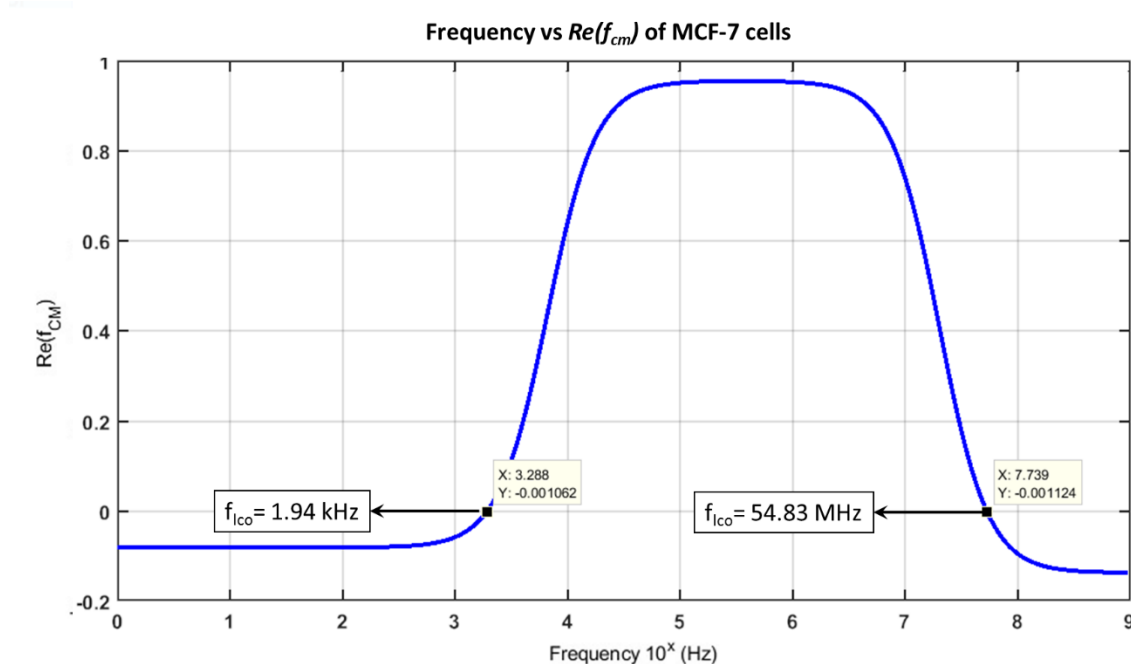


Figure 2.4 DEP spectrum simulation results of MCF-7 cells at the medium conductivity, $\sigma_{med} = 2.5$ mS/m.

A custom-developed MATLAB script was used in order to simulate the $Re(f_{cm})$ value vs. frequency for both MCF-7 and K562 cell lines using Equation (14). The simulation results are shown in Figure 2.4 and Figure 2.5 for MCF-7 and K562 cells respectively. It is observed that the cross-over frequencies appeared at 1.94 kHz and 54.83 MHz for MCF-7 cells and 8.09 kHz and 47.97 MHz for K562 cells in the simulations.

2.5 Literature Survey on Dielectrophoretic Spectra of K562 and MCF-7 Cells

There are many studies that work with dielectrophoretic characterization of mammalian cells using a diverse analysis methodology [38], [40], [49], [52], [61], [62], [65], [72]. Studies that focus on the DEP characteristics of K562 cell line reported the first cross-over frequency (the critical point corresponding to the transition from negative DEP to positive DEP region) between 5 kHz and 100 kHz [40], [49], [52], [73]. The cross-over frequency was reported in this thesis at 200 kHz in correlation with but higher than the previous reports. It is known that the suspending DEP medium has a significant effect on the appearance of the first cross-over frequency [61], [62]. Although these studies used

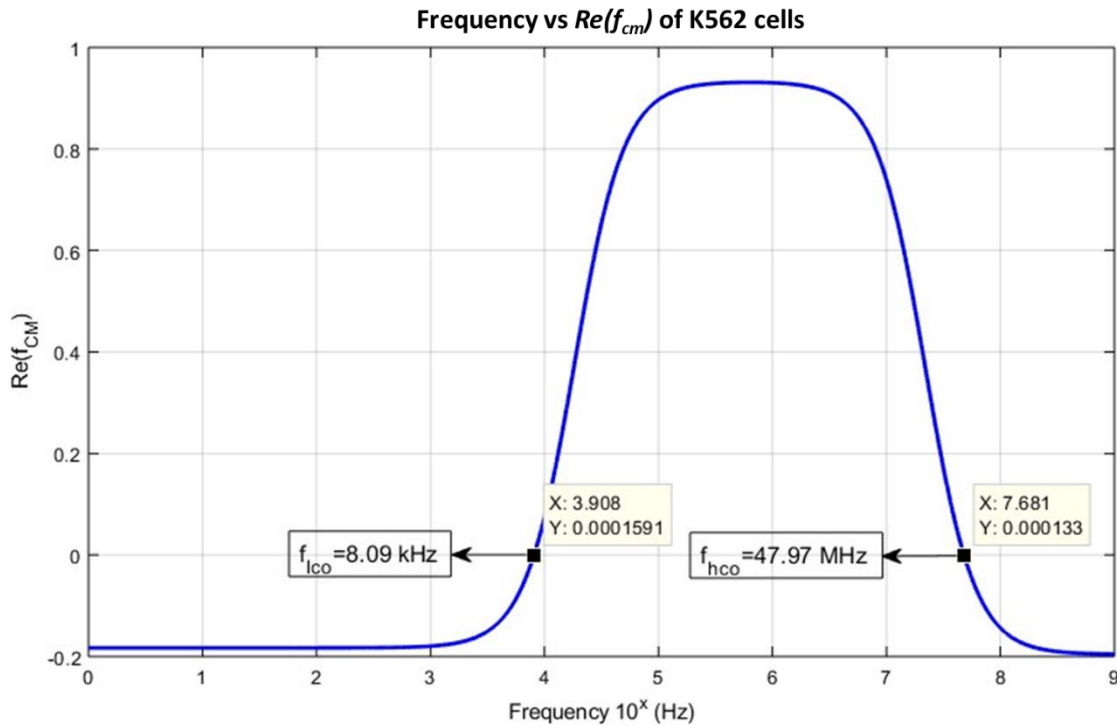


Figure 2.5 DEP spectrum simulation results of K562 cells at the medium conductivity, $\sigma_{med} = 2.5$ mS/m

identical dielectric properties for suspending DEP mediums, they reported disparate results. The divergence in the outcomes have certain reasons. In some studies, rather than experimental results, cell dielectric properties were inserted in cell models to identify the relation between $Re(f_{cm})$ of the target cell and applied frequency [40], [53]. Due to cells' dynamic nature, different dielectric properties have been reported by several research groups in the past [43]. In addition to the divergence in the dielectric property reports, cell modelling introduces assumption based errors. In other reports, cell count or light illumination level was related to the cell characteristics at a certain frequency range [52], [73]. Although, there is a cross-correlation between cell count and $Re(f_{cm})$ data, the correlation level should be carefully investigated in these approaches in order to be used as a strong reference for DEP based cell separation systems that asses cancer on clinical samples. For instance, the effect of cell to cell interaction to the amount of counted cells and to the DEP spectra results should be discussed.

In the aforementioned studies, the high cross-over frequency value (the critical point corresponding to the transition from positive DEP to negative DEP regions) of the K562 cells is not reported, however a significant decrease in DEP force after the frequency of 10 MHz is observed. The DEP spectrum result of K562 cells in this thesis also appears with a significant drop around 10 MHz, and the second cross-over frequency was recorded at 39.8 MHz. MATLAB simulation results for K562 cells modelled with single shell cell modelling approach indicated the second cross-over frequency at 48 MHz. The literature results were grouped in Table 2. It is clearly seen that there is no agreement on the first and second cross-over frequency values reported in these studies.

Table 2 Cell characterization results reported in the literature on K562

	Cell Type	Method	First cross-over frequency	Second cross-over frequency	Drawbacks
[52]	K562	Number of collected cells	– (~ 10 kHz)	– (decrease after 8 MHz)	Weak relation to the DEP spectra
[73]	K562	Number of collected cells	– (~ 7 kHz)	–	Weak relation to the DEP spectra
[49]	K562	Cell conductivity measurements	30 kHz - 90 kHz	–	Weak relation to the DEP spectra
[40]	K562	Cell modelling sim.	10 kHz	48.64 MHz	Dielectric assumptions
Sim.	K562	Cell modelling sim.	8 kHz	48.0 MHz	Dielectric assumptions

Several studies had been conducted on characterization of MCF-7 cells, on the other hand similar to results of K562 cell characterization, there are disparate outcomes in these reports [38], [49], [53], [54], [69], [74]. The first cross-over frequency for MCF-7 cells were reported between 10 Hz to 500 kHz, however the majority of the reports were concentrated on 20 kHz to 100 kHz. Only one of these studies reported the first cross-over frequency above 150 kHz [38]. In this study the characterization results demonstrate very high divergence and DEP force was given in arbitrary units. In addition the results in the corresponding study was not fitted into a DEP model because of lack of correlation. Another DEP related study reported characterization results of MCF-7 cells based on calculations at different solution conductivities (i.e. 1.2×10^{-4} S/m to 7.6 S/m) [75]. However the solution conductivities were either very high or very low. Therefore, it could not be compared to any DEP characterization study in the literature to our knowledge. In addition, the second cross-over frequency did not appear in their results. An extensive study that measures conductivities of variety of cells to calculate the cross-over frequencies (not the whole DEP spectra) reported the first cross-over frequency of MCF-7 cells in between 30 kHz and 70 kHz [49] and another cell modelling study obtained the frequency at 30 kHz [53]. In this thesis, the first cross-over frequency of MCF-7 cells were reported at 100 kHz, in correlation with the aforementioned studies. A study that focuses on the separation of malignant human breast cancer epithelial cells from healthy epithelial cells using dielectrophoresis, calculated a factor called CPS (crucial parameter of separation, $r^3 Re(f_{cm})$) [54]. They only shared calculation results after 1 MHz and reported the second cross-over frequency at 36.2 MHz. The sum-up version of the literature survey on dielectrophoretic characterization of MCF-7 cells were shared in Table 3.

Table 3 Cell characterization results reported in the literature on MCF-7

	Cell Type	Method	First cross-over frequency	Second cross-over frequency	Drawbacks
[38]	MCF-7	V-shaped electrodes (force in a.u.)	280 kHz	20 MHz and 50 MHz	Position dependent force field + Weak theoretical explanations
[54]	MCF-7	Cell modelling sim.	-	36.18 MHz	Dielectric assumptions
[49]	MCF-7	Cell conductivity measurements	30 kHz - 50 kHz	-	Weak relation to the DEP spectra
[53]	MCF-7	Cell modelling sim.	20 kHz	(drop after 10 MHz)	Dielectric assumptions
Sim.	MCF-7	Cell modelling sim.	2 kHz	54.8 MHz	Dielectric assumptions

The decrease in positive DEP force after a few MHz is reported in other cell characterization studies that worked on various cancer cell lines as well [54], [72]. On the other hand, another study, that focused on high frequency region in the DEP spectra analysis of mouse lymphocytes, reported the cross-over frequency at around 200 MHz [76]. The study used cell modelling results of a different study [77] on dielectric properties of mouse lymphocytes as a predictive guide. A possible reason for the divergence in the second cross-over frequency results is that the corresponding study focused on a different cell type (i.e. mouse lymphocytes). The DEP characteristics of lymphocytes are reported

to be different than NCI-60 cell types (human tumour cell lines), hence the second cross-over frequencies are possibly disparate for these two cell types [49]. In addition, in the corresponding study the selected predictive guide is possibly out-dated, considering the dynamic behaviours of cell physiology.

It is clearly seen that in order to obtain DEP spectra of cells, simulations that uses dielectric properties and weak relations on measurement tool and DEP force result in an inconsistency in the results. Considering the throughput requirement of DEP separation systems, this inconsistency cannot be acceptable. Therefore, a direct relation between experimental measurements and DEP spectra (hence DEP force) should be established. This thesis is aimed to obtain an accurate DEP characterization system to obtain $Re(f_{cm})$ at any frequency experimentally, hence directly.

CHAPTER 3

DESIGN, SIMULATION AND FABRICATION OF THE DIELECTROPHOTRETIC CHARACTERIZATION DEVICE

The main purpose of this study is to obtain a dielectric cell characterization method that does not depend on assumptions based on cell modelling and dielectric properties. Therefore, a microfluidic DEP characterization device is designed, fabricated, tested and analyzed. This allows to obtain DEP spectra of a cell experimentally. This chapter is dedicated to present the design, electric field simulations, constructed analysis methodology, and fabrication of the DEP characterization device, through explaining each step in details.

3.1 Electrode Configuration and Device Design

Electrodes are responsible for the generation of the non-uniform electric field. Hence, the electrode configuration plays a very crucial role in the direction and magnitude of the generated DEP force, taking the form of $\nabla|\vec{E}_{rms}(r, \omega)|^2$ in Equation (1). The main design specification in electrode configuration is to obtain the force field, $\nabla|\vec{E}_{rms}(r, \omega)|^2$ uniform and unidirectional. However, this is a tough challenge since the field is highly position dependent because of the gradient operations as expressed in Equation (9).

3.1.1 *V-shaped planar electrode*

In our group, a DEP characterization chip was already designed and fabricated. The design specification were inspired from a study conducted by F. Yang et al. [78]. In Figure 3.1

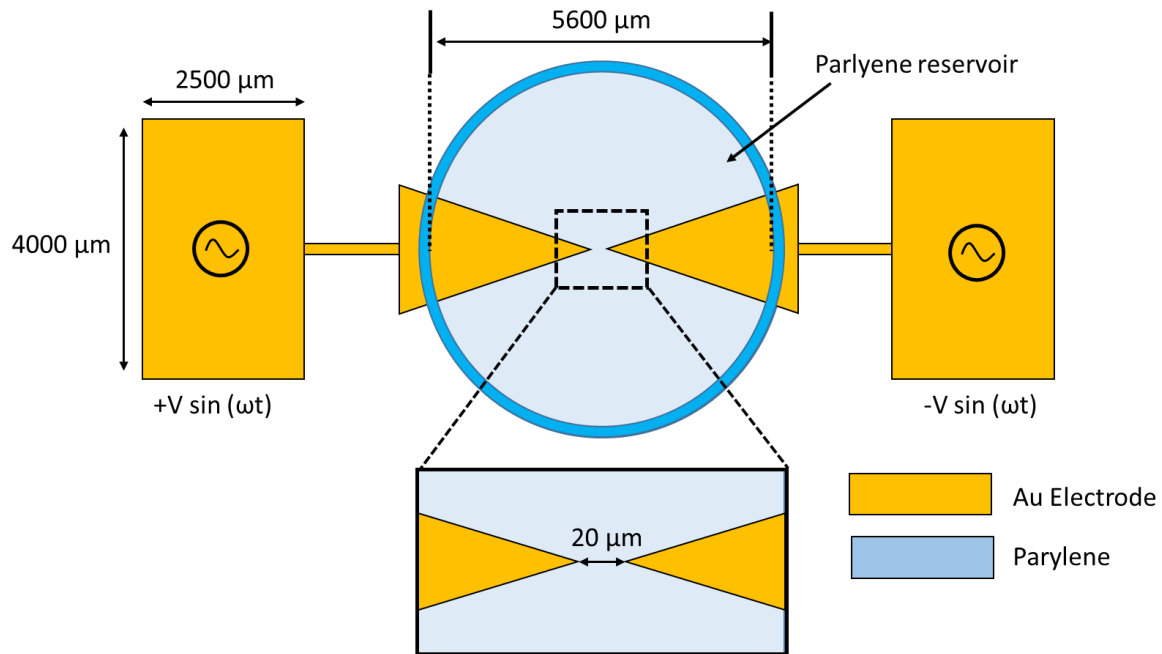


Figure 3.1 The electrode and channel configuration of the initially fabricated DEP characterization devices in BioMEMS research group [79].

the constructed geometry is presented [79]. There are two reciprocal V-shaped planar electrodes with a 30° angle between the edges. The gap between the electrode tips is $20\ \mu\text{m}$. A parylene reservoir ($h=20\ \mu\text{m}$) was used to confine the cell solution. A final parylene coating was done to provide electrical insulation of the electrodes and to eliminate electrolysis in the tested frequency range.

The structure was re-created in 3-d on COMSOL Multiphysics and parameters were defined for each structural component (i.e. parylene, DEP suspension and metal) as illustrated in Figure 3.3. Planar electrode structure was selected in fabrication as it is easier to realize than 3-d metal electroplating. Therefore, because of the asymmetry in the z-axis, the electric field divergence in the z-axis should also be taken into account in the force field calculations. Electrostatic simulation result at x-y plane of $\nabla|\vec{E}_{rms}(r, \omega)|^2$ factor at $z = 5\ \mu\text{m}$ when 10Vpp at 1MHz with a 180° phase difference was applied to the electrodes, is shown in Figure 3.2.

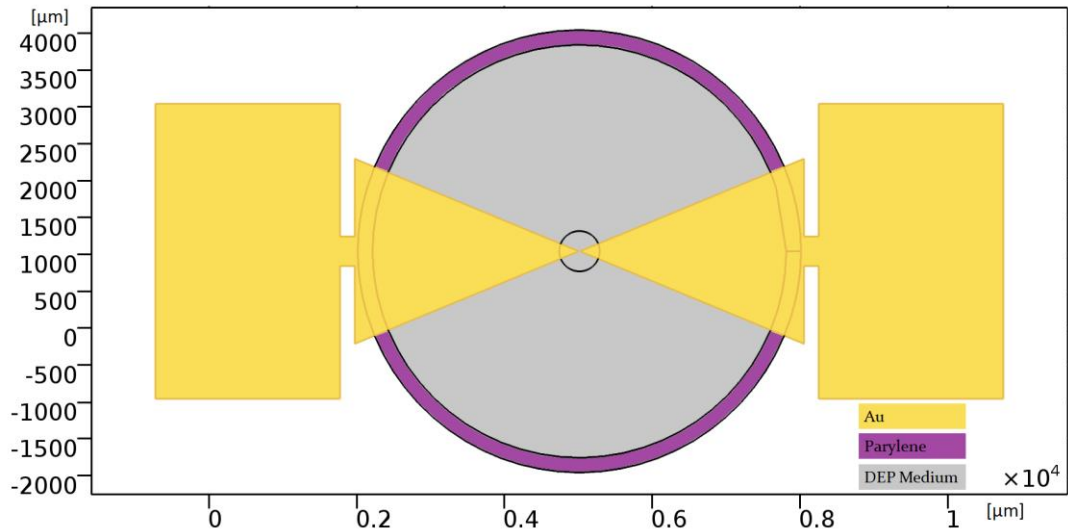


Figure 3.3 COMSOL modelling and material definitions.

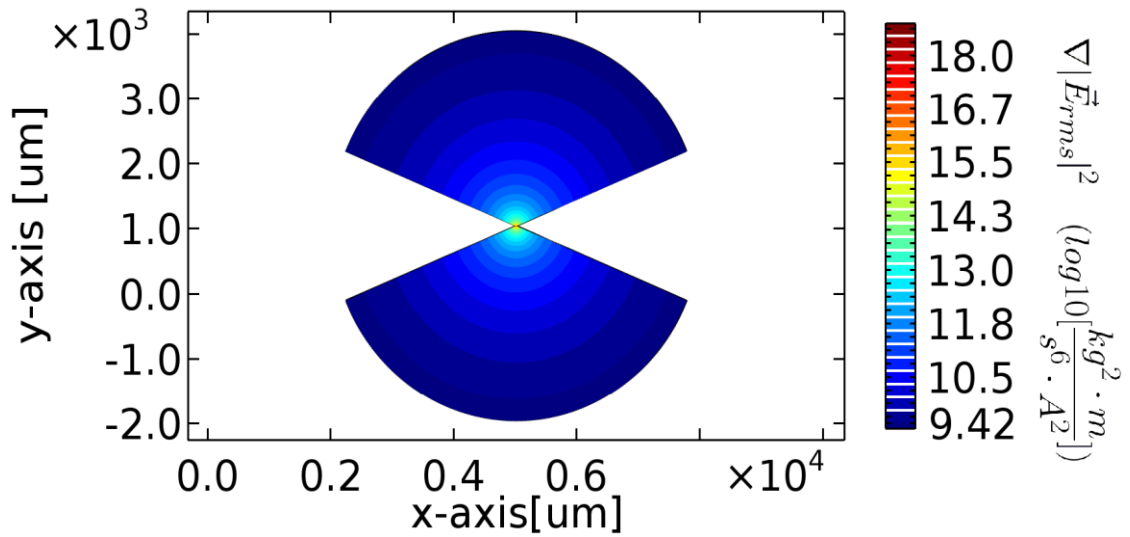


Figure 3.2 Electric field simulation results of the overall geometry, where $\nabla|\vec{E}_{rms}(r, \omega)|^2$ results are illustrated. It is observed that the force field is not uniform.

As cancer cells are a few microns ranged particles, to track their trajectories accurately, it was zoomed to a $400\mu\text{m} \times 400\mu\text{m}$ region as shown in Figure 3.5. The effect of z-component is illustrated in Figure 3.4, where arrows correspond to the direction of the positive DEP force. Since near electrode tips and sides DEP force direction and magnitude

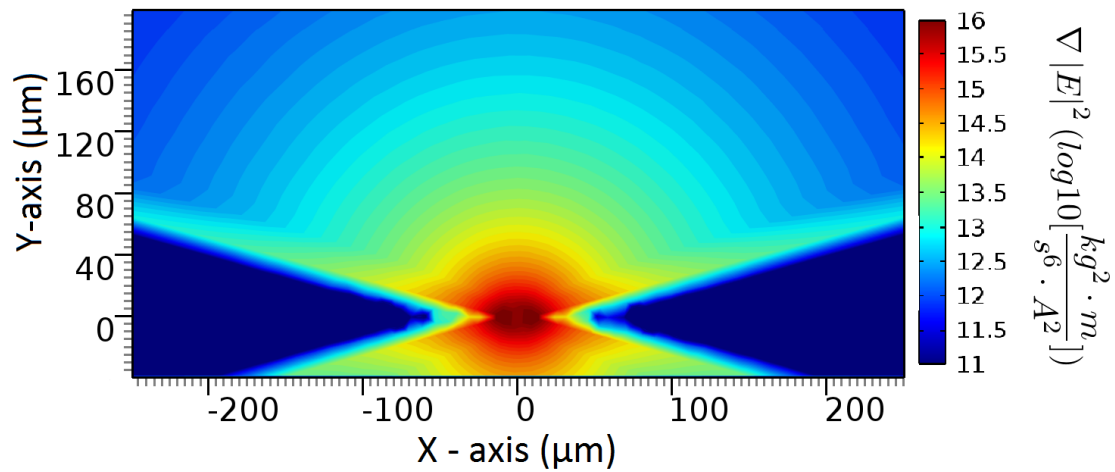


Figure 3.5 Electric-field simulation results of the analysis region (400 μm x 400 μm) box. Only half of the box is shown due to symmetry.

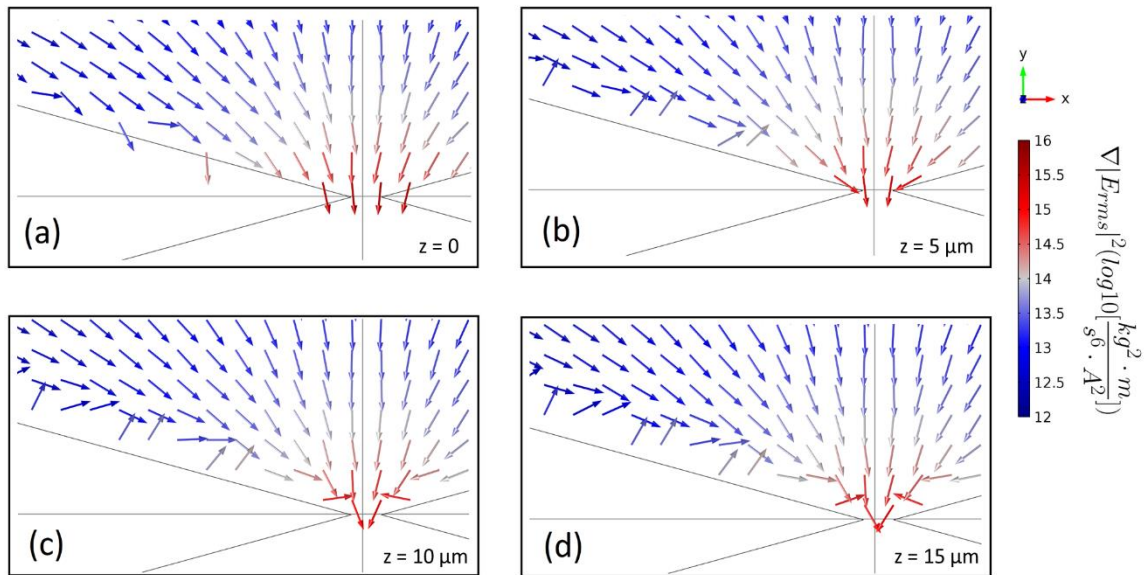


Figure 3.4 Electric-field simulation results at different heights. It is seen that z-axis has an effect on the field direction and magnitude near the electrodes.

varies in the order of magnitude of 3, cells that are located at least 100 μm further than the electrodes were analyzed.

The simulation results show that electric field gradient component appearing in Figure 3.5 is strongly position dependent. As discussed previously, in order to get rid of high

mathematical expression that is introduced in the solution of Equation (11), the electric field should be isomotive. Meaning that $\nabla|\vec{E}_{rms}|^2$ should be uniformly distributed in the microchannel. In addition, the electric field simulations indicate a graduation in the z-axis, which brings another complexity dimension and was ignored for the sake of complexity. On the other hand, since the fluid height inside the reservoir is changing because of the fluid mechanics, therefore taking a constant z-value in $\nabla|\vec{E}_{rms}|^2$ is also problematic. Therefore the electrode configuration is optimized in order to obtain isomotive E-field with z-axis independency.

3.1.2 Electrode Configuration Evolution for Isomotive Electric Field Generation

First of all a circular electrode and a vertical electrode were placed opposing each other and the electric field flux generated in-between was examined by applying 10V_{pp} signal to both electrodes with 180° phase difference. The inner radius of the first circular electrode and the distance in between the two electrodes were parametrized and COMSOL Multiphysics parametric sweep simulations were conducted for a range of values of the parameters. E-field gradient was changing smoothly and slowly, as shown in Figure 3.6, yet DEP force was not appeared to be in the same direction in whole active DEP region, complicating to define a particle trajectory throughout the tests.

To understand the effect of curvature to the flux lines, vertical electrode was replaced with another circular electrode and same simulations were repeated by sweeping all the combinations from 50μm to 2500μm circle radius for both electrodes. The most uniform result gathered from the simulations is shared in Figure 3.7. The performance in this case was better than circular-vertical electrode configuration. However, the field direction was again pointing the middle of the chip. This is problematic as particles that are located in the middle may feel no force at all, and collisions may happen as they pass through the middle point.

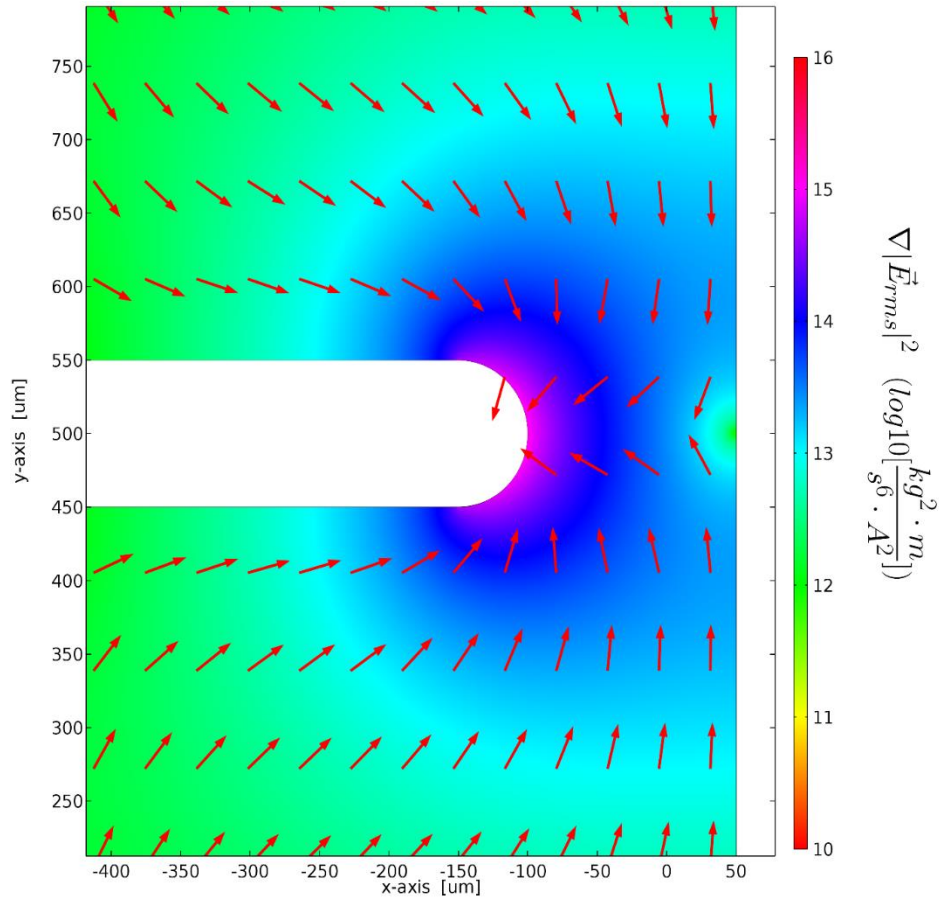


Figure 3.6 Electric-field simulation results of circular vs. vertical electrode configuration

In order to direct all particles in one direction (i.e. direct them to one of the electrodes), electrode configurations were modified. A parametric sweep was conducted sweeping all of the combinations for the radius values of the circular electrodes. The parametric sweep results of the simulation is shared in Figure 3.8. The optimum values were selected to be fabricated after slight modifications to fit in a microchannel device and shared in the next subsection.

3.2 Finalized Electrode Configuration and the Microchannel Design

Concave-convex combination proved to be supplying both uniform and unidirectional force field. The proposed system in this thesis is composed of a one-sided convex (2600

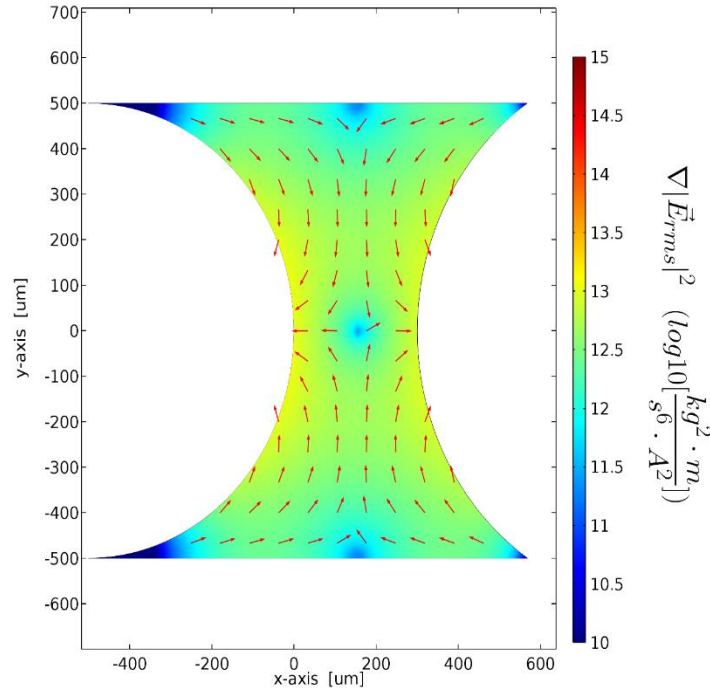


Figure 3.7 Electric-field simulation of concave electrodes opposing each other.

μm diameter) metal (i.e. gold) opposing a one-sided concave (2000 μm diameter) metal. The separation between the electrodes are 350 μm , large enough to analyze cell motion. The microchannel having a width of 500 μm and a length of 16 mm, was designed with 20 μm thick parylene walls and circular inlet and outlet ports (1500 μm diameter). The gold electrodes were placed in the middle of the microchannel. The final device structure and its dimensions are given in Figure 3.9.

Design parameters of the electrode configurations were simulated using a three-dimensional model created using the AC/DC module of COMSOL Multiphysics software (version 5.1) in order to verify uniform, gradually varying (i.e. 0.5%/ μm), and direction controlled $\nabla |\vec{E}_{rms}|^2$ generation by isomotive electric field.

Throughout the electric field simulations, DEP medium suspension conductivity (σ_m) and permittivity (ϵ_m) were defined as 2.5 x mS m^{-1} and 78 ϵ_0 , respectively, based on the measurements with a conductivity meter (PP-50, Sartorius AG, Germany). A parylene C layer (500 nm thickness, σ_m and ϵ_m are 2.5 x 10⁻¹⁵ S m^{-1} and 3.15 ϵ_0 , respectively) was

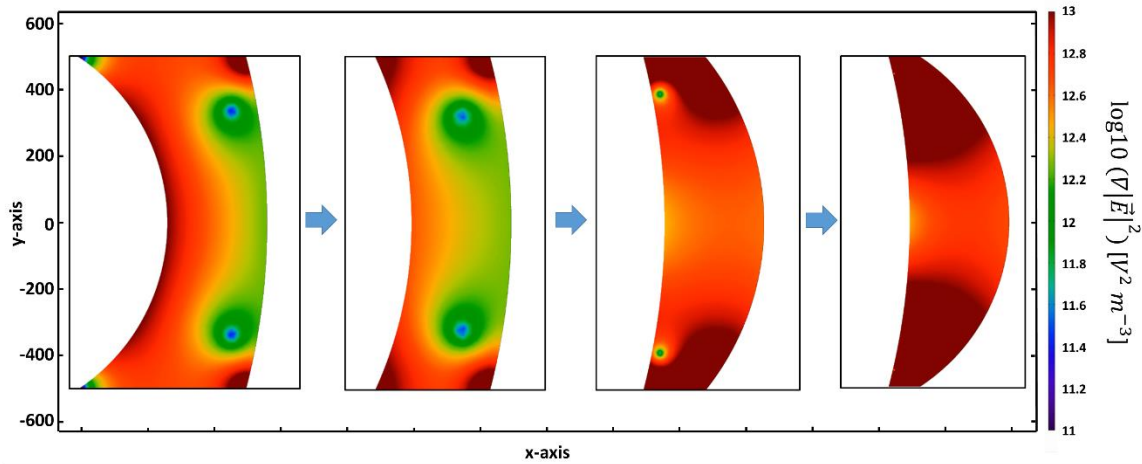


Figure 3.8 Electric field simulations of concave and convex electrodes facing each other with different radii. The radius values were swept and the results are illustrated in the figure.

defined on top of the electrodes for insulation purposes and to prevent electrolysis of the fluid. An active region of $260 \mu\text{m} \times 200 \mu\text{m}$ was selected for cell monitoring as shown in Figure 3.10. Simulations were conducted with a three-dimensional model created using the AC/DC module of COMSOL Multiphysics. The electrodes generate a gradually varying and uniform force field in the selected region. As can be seen from the figure legend, the force field is varying between 0.9×10^{12} and $1.8 \times 10^{12} \text{ [V}^2/\text{m}^3]$. Arrows in the figure illustrate the direction of the generated positive DEP force. The force direction is also illustrated in the same figure, where cells having positive Clausius-Mossotti factor

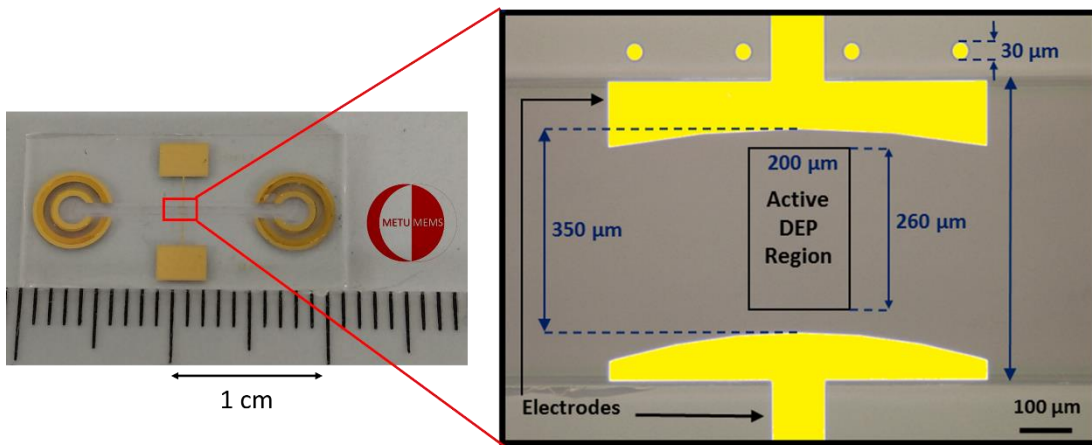


Figure 3.9 The fabricated device and device dimensions

are attracted towards the convex electrode. It is also verified that rather than a three-dimensional electrode structure, a planar electrode configuration (easier to realize) is satisfactory as force field is independent of z- axis in the selected region as shown in Figure 3.10c.

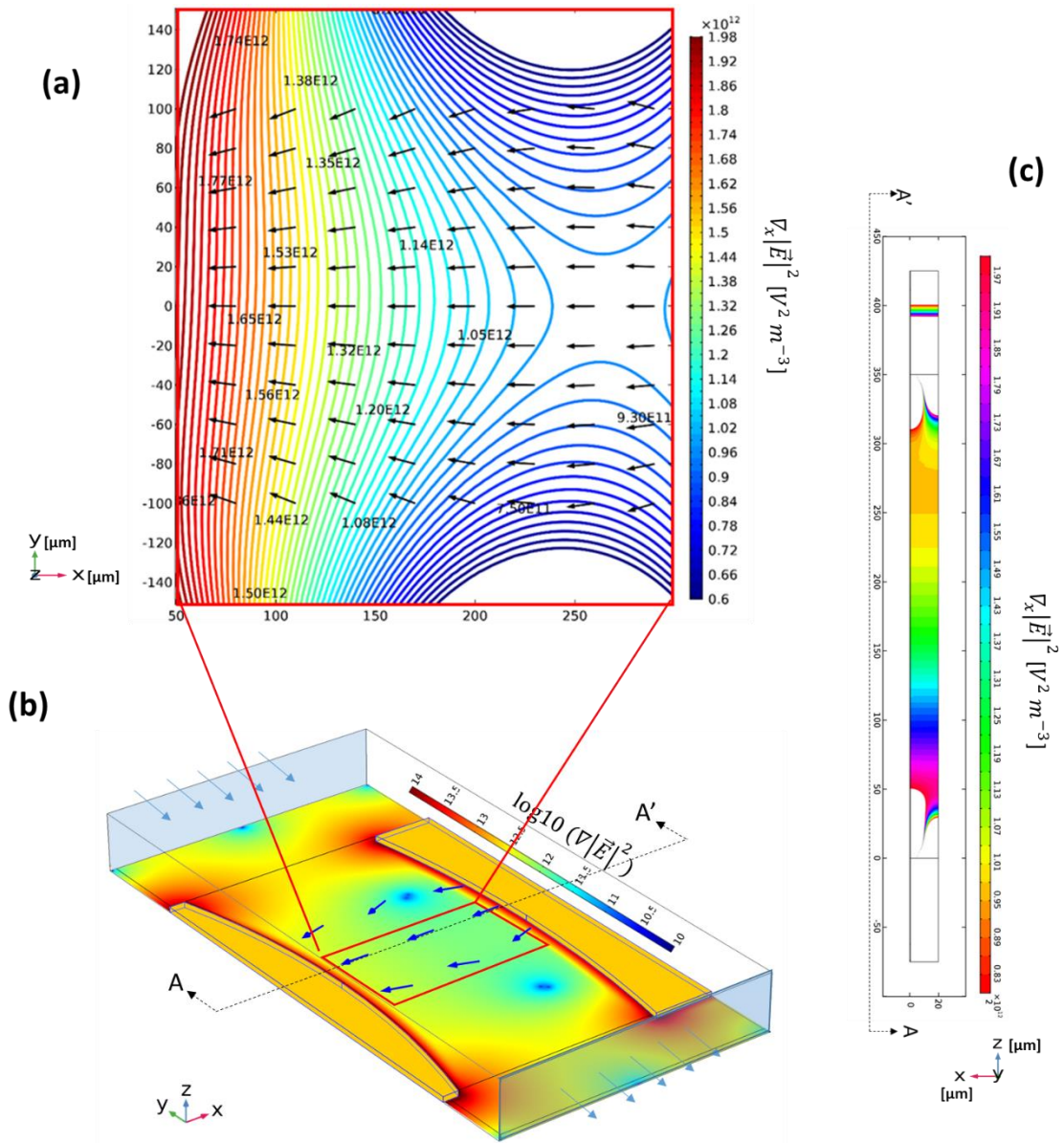


Figure 3.10 $\nabla|\vec{E}|^2$ (force field) simulation and electric field fitting results. (a) The isomorphic behavior of the electric field for the active monitoring region (on x-y plane at $z = 10\mu\text{m}$, half of the channel length). (b) Schematic of the microfluidic device. (c) Distribution of the force field in x-z plane (at $y = 0$).

3.3 Analysis Methodology

The analysis methodology is very critical in this study. The main purpose of this thesis is to obtain DEP spectra experimentally. Therefore, a relation between the experimental observations and $\nabla|\vec{E}_{rms}|^2$ calculations should be established, supported with a theoretical basis. Since the designed electrodes are capable of generating isomotive field inside the channel, this relation becomes possible.

Since $\nabla|\vec{E}_{rms}|^2$ is not highly position dependent, Equation (11) is simplified from highly complex mathematical calculations. With the knowledge of $\tau_a = m_p/6\pi\mu R$ being much smaller than the time scale of the variation of the electric field variables, the acceleration of the particles then can be neglected [55]. Therefore, in a slowly varying or position independent force field, caused by an isomotive electric field, solution of Equation (11) for particle velocity can be obtained as,

$$\vec{u}_p = \left(\vec{u}_0 - \vec{u}_m - \frac{\vec{F}_{DEP}}{\gamma} \right) e^{-(6\pi\mu r/m_p)t} + \vec{u}_m + \frac{\vec{F}_{DEP}}{6\pi\mu r} \quad (16)$$

Exponential term in Equation (16) can also be neglected for an isomotive electric field, hence cell velocity can be obtained after replacing the corresponding variables and constants as [55], [80], [81],

$$\vec{u}_p = \vec{u}_m + \frac{\varepsilon_m r^2 Re(f_{cm}) \nabla|\vec{E}_{rms}(r, \omega)|^2}{3\mu} \quad (17)$$

If the fluid medium is stationary, in other words \vec{u}_m is equal to zero, $Re(f_{cm})$ factor, which is characteristic to each cell type, can be obtained as (i.e. using x-direction components of the vectors),

$$Re(f_{cm}) = \frac{3\mu u_{px}}{\epsilon_m r^2 (\nabla_x |\vec{E}_{rms}(r, \omega)|^2)} \quad (18)$$

Notice that all parameters on right hand side of Equation (18) can be obtained or controlled in a microfluidic system. The design of the electrodes enables obtaining $Re(f_{cm})$ values of target cells using Equation (18) without going through highly complex mathematical calculations. Therefore, it is possible to obtain DEP spectra of living cells by accurate determination of these parameters and without ascertaining cell membrane and cytoplasmic properties.

3.4 Electric Field Fitting with MATLAB

Throughout the electric field simulations triangular surface meshing with maximum element size set at 3 μm and other element size parameters set at their default values (calibrated for General physics, extremely fine meshing) was swept to the whole body with Quadrilateral face meshing method having 40 distribution elements in COMSOL Multiphysics as illustrated in Figure 3.11.

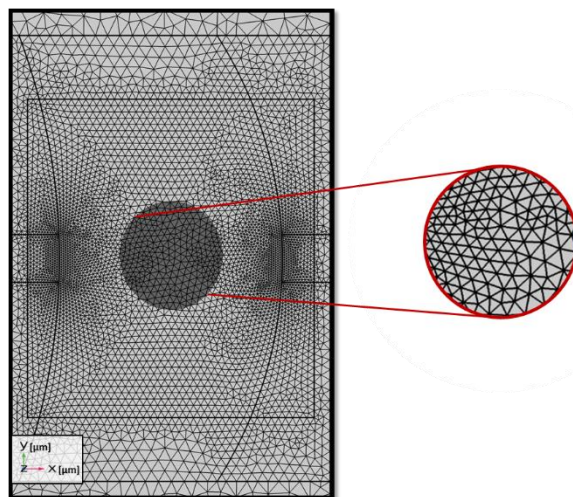


Figure 3.11 Triangular surface meshing with maximum element size set at 3 μm and other element size parameters set at their default values (calibrated for General physics, extremely fine meshing) was swept to the whole body with Quadrilateral face meshing method having 40 distribution elements in COMSOL Multiphysics for electrical simulations.

As given in Equation (18) at each time lapse (defined by the video recording frame rate) electric field gradient value at the specific cell location should be taken from the simulations. After capturing cell motion, the frames were post-processed both in Android software and in MATLAB to extract $Re(f_{cm})$ data. On the other hand, the COMSOL data consists of spatially random field data, and does not cover every single point in the physical device domain. In order to use the data in the analysis in fully autonomous fashion, force field simulation results were extracted from COMSOL domain, reconstructed and fitted in MATLAB platform to a square mesh with $1 \mu\text{m} \times 1 \mu\text{m}$ size. Therefore, the field data was registered with pixel coordinates of the cell video in the active analysis region as illustrated in Figure 3.12. This procedure was conducted by M. Kamil Aslan.

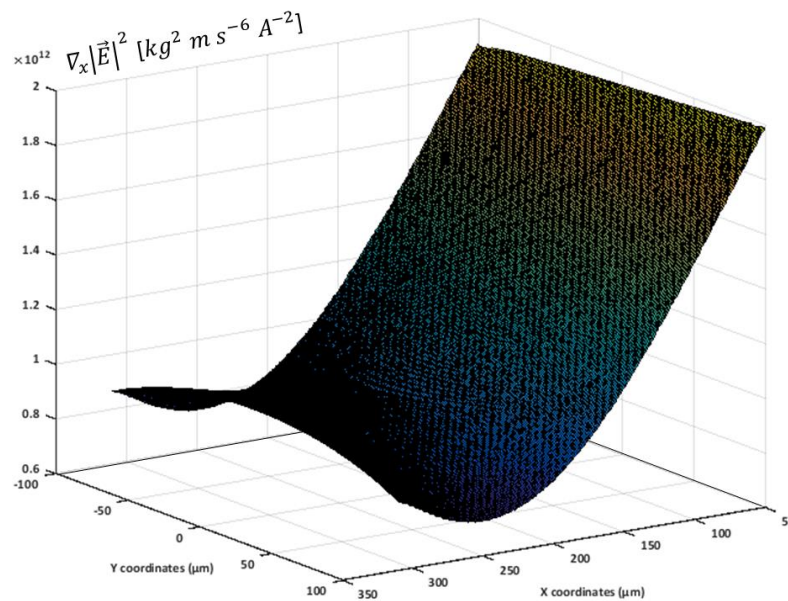


Figure 3.12 Square fitting of triangular mesh with $1 \mu\text{m} \times 1 \mu\text{m}$ dimensions. Magnitude of the x-component of the force field extracted from COMSOL simulations fitted in MATLAB platform in x-y domain is shown on z-axis of the illustration.

3.5 Fabrication

In the fabrication of the proposed micro-device, as to accomplish one of the objectives in this thesis (obtaining a cheap and disposable microchip), standard and straightforward microfabrication tools were utilized including a cost-effective and flexible polymer, parylene-C. The fabrication flow for the DEP characterization devices is shared in Figure 3.13. This process is a 3-mask process and the masking structures are illustrated in Figure 3.14.

Glass Wafer was selected as the basis substrate, since it enables observations from both perspectives (bottom and top of the device). As a first step, a thin film titanium layer with high adhesion and a gold layer to form planar electrode structure (30 and 300 nm thickness, respectively) were sputtered (AJA-International Inc., USA) on a 6" glass wafer. Metal structure was patterned by wet etching (SPR™220 photoresist used for masking,

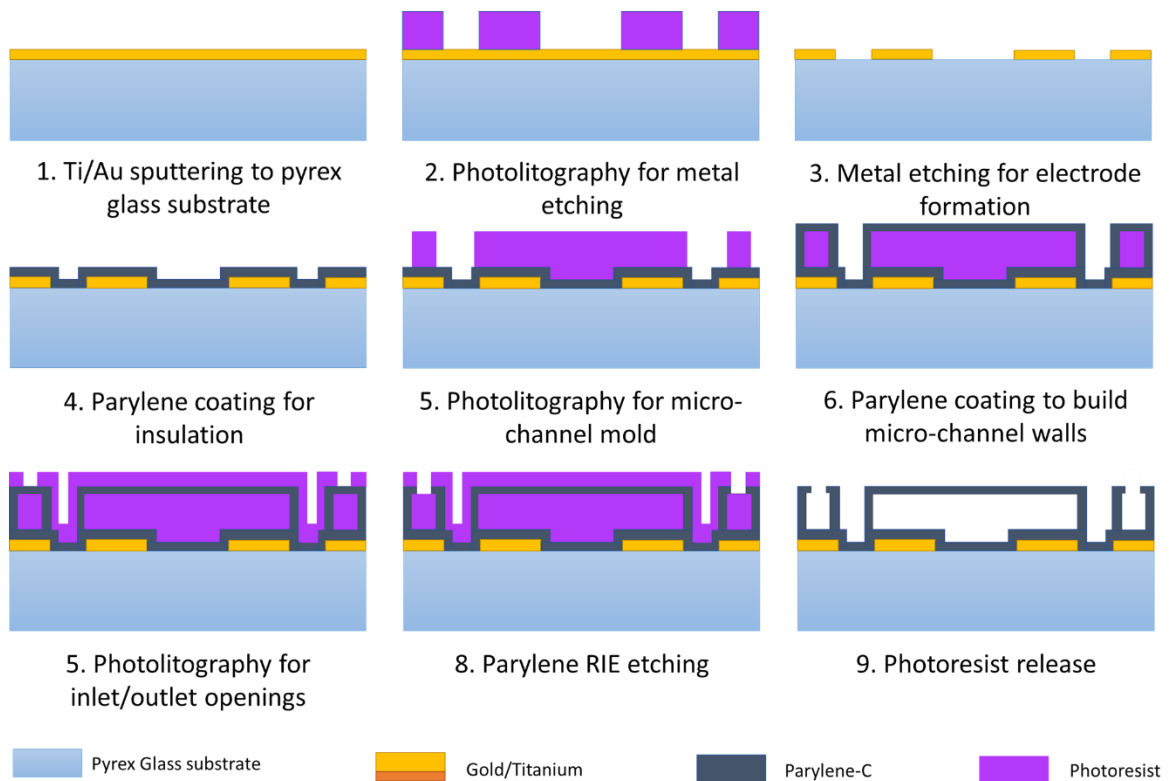


Figure 3.13 Fabrication flow of the DEP characterization device.

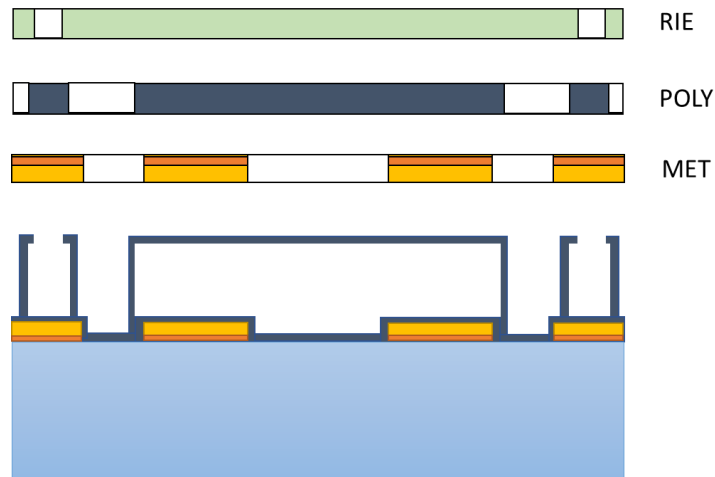


Figure 3.14 The fabrication masks for PR patterning.

EVG 620 Precision Alignment, Austria). Next, the wafer was coated with parylene-C film (500nm thickness, Labcoter® 2, SCS, Inc., USA) for insulation purpose. A second lithography process was done with spin-coating AZ® 40XT-11D photoresist and continued with a 20 μm parylene-C coating for channel formation. Channel inlet and outlet, and electrode panel openings were created with reactive ion etching (RIE) process (ICP-RIE, SPTS, England). Remaining PR inside the channel was released with acetone, isopropyl alcohol, and ethanol cleaning (5 days, 30 min., 30 min., respectively, and 20 min. on hot plate at 60°C) prior to testing.

In the testing of parylene based microchannel some challenges and obligations were observed. A more detailed explanation of the problem and a discussion about the solution phase is given in at the end of this chapter. In order to overcome the obligations and issues, a different material combination is tested through the aforementioned fabrication steps, where parylene channel step was eliminated. In order to ease the fabrication steps, to have more fabrication-independent control on the inlet and outlet sizes, and to achieve better user-friendly control in the flow rate inside the channel, PDMS channel is planned to be implemented instead of parylene. Same microfabrication masks were used to create a PDMS mold, with 20 μm channel height, to be positioned on top of the pre-designated locations. Several tests were made to stick PDMS on parylene layer. Although some tests

performed better results, following the introduction of a liquid to the microchannel, fluid leakages were observed in all of the trials after a certain level of inlet pressure. For this reason, the designated problem is postponed to be studied in the future.

CHAPTER 4

EXPERIMENTATION, RESULTS AND DISCUSSION OF THE DIELECTROPHORETIC CHARACTERIZATION DEVICE

The main objective is to obtain an automated, rigorous and unbiased testing procedure in order to minimize human based errors in the calculations. In section 4.1, the constructed experimentation procedures, including a discussion between the relation between cell morphology and dielectric properties were presented. In section 4.2, DEP spectra results of both MCF-7 and K562 cells were given. In section 4.3, a complete discussion with the literature is shared. In addition the verification of the analysis model is given in this chapter.

4.1 Testing

The importance of automation in testing is discussed before, as it minimizes the human-based errors. In addition, achieving a portability is also a goal, since it enables testing in resource limited regions as well as gives flexibility to the user. This section contains two different testing procedure, where the first one uses microscopy block for video recording and MATLAB for post-processing the recorded videos. In the second procedure, the portability was achieved by integrating a portable signal generator and a CMOS image sensor that are compatible with a smartphone through custom-developed Android software. The overall procedure is as follows;

- Preparing the cell solution.

- Introducing the cell solution into the active region inside the microchannel.
- Energizing the electrodes with a sinusoidal signal of $20 V_{p-p}$ having 180° phase differences and record the video of cell motion under this field.
- Obtaining the trajectory of the cells through post-processing the recorded videos, and calculating the velocity and acceleration data.
- Point-by-point cross-matching the cell position with the corresponding $\nabla|\vec{E}_{rms}|^2$ value at that certain location.
- Calculating $Re(f_{cm})$

To start with, since the electrode separations are $350 \mu\text{m}$ multiple cells (located inside the active region) can be analyzed simultaneously. However, cell to cell interactions introduces new force elements that should be taken into account while calculating the net force. In order to simplify the mathematical calculations and equations and to get rid of complex force expressions in Clausius-Mossotti factor calculation, at most 5 cells that are at least 3 times the distance of their radius length apart from each other were analyzed for each experiment. For every single cell, Clausius-Mossotti factor was calculated independently and average value was recorded.

Since the proposed DEP characterization devices were designed as having microchannel structure, it is possible to remove the residual fluid by applying a positive pressure at the inlets of the device. Therefore, prior to each cell tracking, the microchannel was flushed for a certain amount of time, and new solution was introduced to the channel. Each analysis cycle takes at most 30 seconds, which is due to the velocity of the target cell. The preparation cycle on the other hand takes 5 to 10 seconds. Hence the system can theoretically analyze 450 cells in an hour.

4.1.1 Sample Preparation

Throughout this thesis two readily available cell lines, MCF-7 breast cancer cells and K562 human leukemia cells cultured in Biology Department, METU, were used. An isotonic DEP medium (0.3% (w/v) dextrose and 8.5% (w/v) sucrose) with $2.5 \times \text{mS m}^{-1}$ conductivity was prepared [40], [52]. The cells were centrifuged at 1000 rpm for 5 min. and were introduced to the DEP suspension (2.6×10^6 cell/ml). For microscopy tests cell mixture was stained with fluorescein diacetate (FDA, $12 \mu\text{M}$ with cell suspension having 1×10^6 cell/ml concentration, 15 minutes incubation) with green color marking. For the portable LOC system fluorescein marking was not used. Prior to injection to microchannel, cells centrifuged and washed twice with the same DEP medium. Tubing ports were glued to inlet and outlet of the fabricated devices with adhesive epoxy (LOCTITE 1C, Henkel AG & Co, Germany).

Before starting each test, the DEP channel was conditioned with ethanol, DI water flows for 10 minutes each. The cell culture solution was injected to the channel with a pressure driven microfluidic flow control system (MFCS™-EZ, Fluigent GmbH, Germany) and a stationary stage is achieved by arranging the inlet pressure.

4.1.2 Microscopy Tests and MATLAB Post-Processing with MCF-7 cells

Before considering the portability issues, initially an autonomous, hence unbiased test setup was planned for the DEP characterization devices. After maintaining stationary DEP solution inside the channel, cells located at the pre-specified region were examined with an inverted microscope under fluorescence illumination (5x zoom, DMi8 automated, Leica Microsystems CMS GmbH, Germany). A 20 Vp-p sinusoidal voltage at 15 different frequency values between 30 kHz and 50 MHz (4 frequency points for each decade) was applied to the electrodes with 180° phase difference (811501-120 MHz, Agilent Technologies, USA) to generate the desired electric-field flux lines. The cell motion was

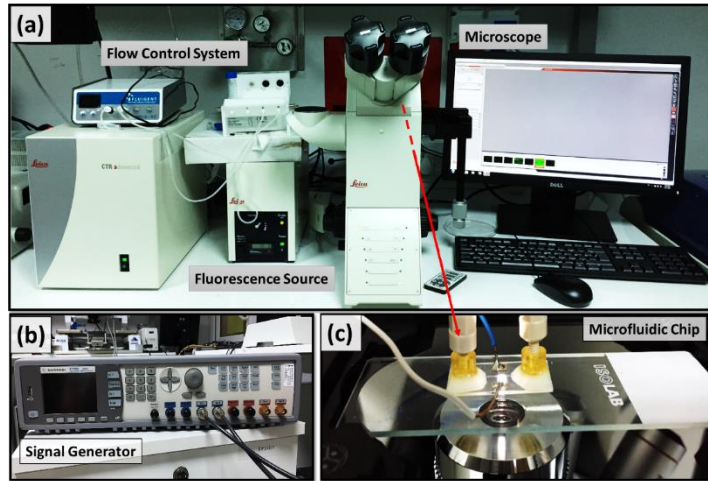


Figure 4.1 The microscopy test setup. (a) Overall test setup including Ratio imaging inverted research microscope at 5x zoom, microfluidic flow control system, fluorescence light source and microfluidic DEP chip (b) Signal generator. 10 V_{p-p} AC signal at 15 different frequencies ranging between 30 kHz and 50 MHz was applied to electrodes with 180° phase difference in between (c) Microfluidic DEP chip.

recorded with an integrated microscope camera (MC190 HD, Leica Microsystems CMS GmbH, Germany) controlled by Leica Application Suite (version 4.8.0) using FITC filter cube (Ex: 400 nm). The microscopy test setup is shown in Figure 4.1.

A custom MATLAB application and graphical user interface (GUI) was developed by M. Kamil Aslan to post-process videos in autonomous fashion. Figure 4.2 shows the custom designed GUI for processing of the recorded experiment videos and snapshots to calculate $Re(f_{cm})$ value.

The workflow of the MATLAB application is summarized below.

Image Sampling and Enhancement

Cell videos were read and sampled into image frames with 30 fps. Then, the images were converted from colored scale to grey scale and enhanced by employing adaptive histogram equalization. To eliminate pixel noise, median filtering with a 2x2 kernel size was applied.

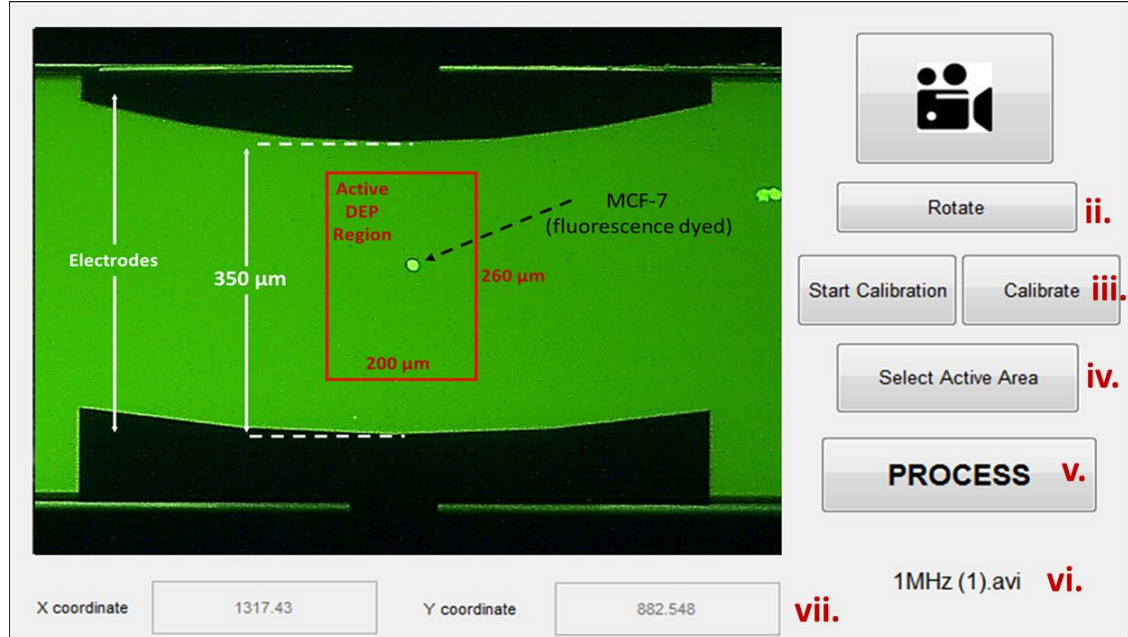


Figure 4.2 Video processing with MATLAB. (a) MATLAB GUI for investigation of recorded cell motions. The procedure is as follows; i. Video selection. ii. Video rotation (if necessary) for consistency in x-y domain definitions. iii. Selection of concave electrode tips for automatic tilting and pixel to metric calculations. After clicking on ‘calibrate’ button the previously dedicated cell tracking area appears. iv. User dedicated selection of active cell monitoring area. v. Start of frame by frame video processing for cell tracking. vi. Selected video name. vii. Selected calibration point coordinates.

Theta Alignment of frames

To eliminate theta tilting difference caused by microchip position inside the microscopy holder and the camera angle, samples frames are required to be tilted and aligned. In addition, system should be introduced with a distance/pixel ratio to match COMSOL simulation data with the cell trajectory. For this reason, the known distance between concave electrode tips were used, where the tips were selected by the user at the beginning of each video and then angle of the line connecting the tips was determined and the frames were rotated until this line became horizontal. This procedure also eliminates the cases in which the microchip is placed 180° rotated.

Analysis Area Selection

As discussed before, an analysis region was determined through which the electric-field simulation results show the most isomotive behavior (i.e. $\nabla|\vec{E}|^2$ is changing gradually) and DEP force is unidirectional (i.e. towards one axis crossing center of both of the electrodes). Since pixel to pixel distance was converted to micron domain using position data of the electrode tips, the analysis area was automatically segmented using spatial relationship. Then the cropped frame was replaced with the whole video frame to be shown in the GUI.

Cell Tracking

Cells inside the active area were tracked using a Hough Transform based algorithm. Initially, the image was binarized and filtered with a certain threshold value. The threshold value was arranged automatically through Gaussian distribution of pixel illuminations. Since cells do not have exact circular shapes and sometimes show physiological defects, circular recognition results in dislocations and mismatches. In this manner, a filling algorithm is applied to every hole and the cells were detected using Hough Circle Detection. The cell tracking between each frame was overcome based on spatial neighborhood relationship, where the program compares the center of the already recognized cell in the previous frame with the current frame and checks if the distance is

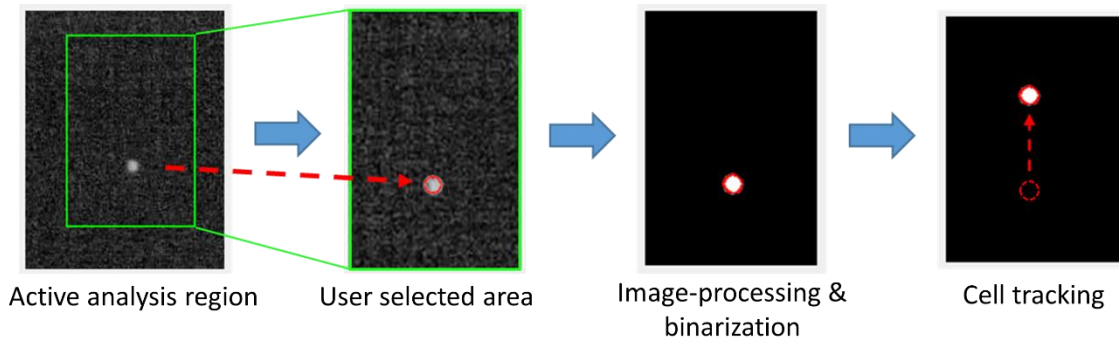


Figure 4.3 Previously dedicated cell tracking area appears after calibration is completed. Green square corresponds to the user selection for active monitoring area, where program automatically zooms to the new area. Video is read and sampled into frames with 30 fps rate. Then images were converted into greyscale followed by adaptive histogram equalization, 2-D median filtering, and binarization by thresholding steps.

smaller than a certain value (in the case of correct matching, this distance is the covered path by the cell at a 1/30 second interval). The process snapshots is shared in Figure 4.3.

For each frame, center coordinates of each tracked cell and cell radii were recorded. The trajectory points were fitted to an equation using third order polynomial fitting. By taking derivative of the fitted equation with respect to time, cell velocity was obtained. Electric-field simulation data fitted to MATLAB domain was added for each corresponding center coordinate for each frame. Using velocity, radius and $\nabla|\vec{E}|^2$ data in Equation (18), average Clausius-Mossotti factor for each cell at each frequency stop was calculated.

4.1.3 Cell Characteristics Deviation According to Cell Morphology

In order to understand the relation between DEP characteristics and cell morphology, in other words, in order to create a ground truth basis to detect the correct target cells, 20 identical tests were conducted. The tests were done with K562 cells where 20 Vp-p sinusoidal voltage at 1 MHz with a 180° phase difference applied to the electrodes. Prior

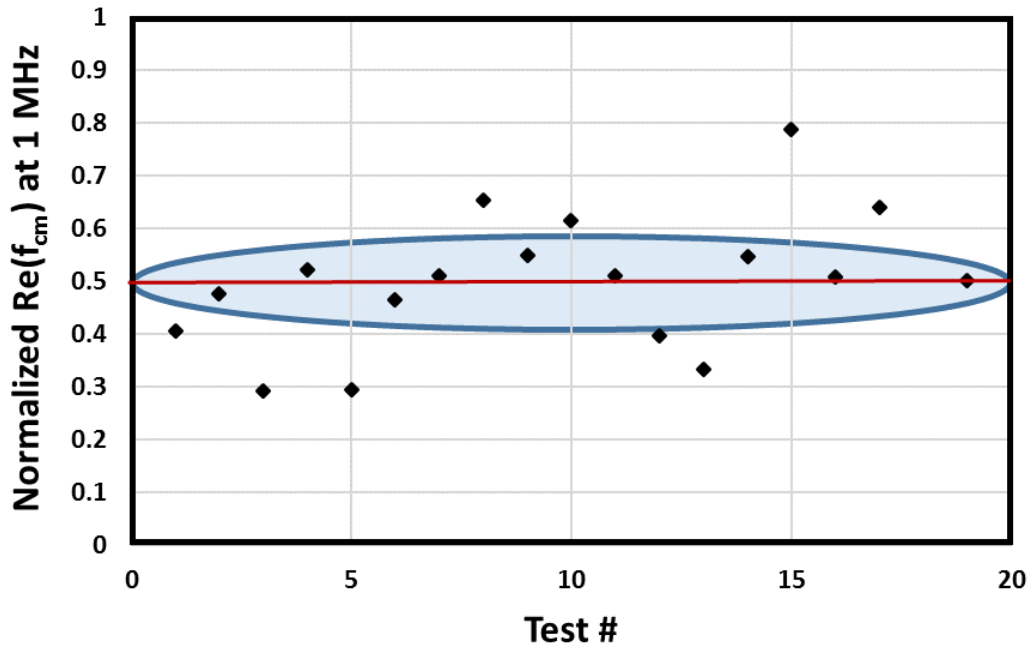


Figure 4.4 Correlation between the test results of K562 cell line. Area inside the blue ellipses shows that the majority of the cells in the range from 0.4 to 0.6. Red line is drawn at 0.5, showing the average.

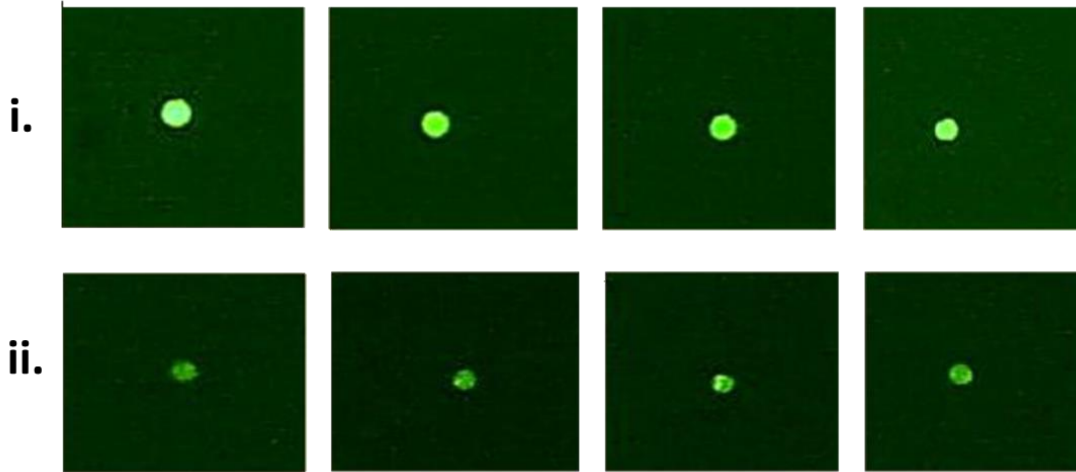


Figure 4.5 Target cells used in DEP spectrum investigation. i. Cells exhibit the average DEP characteristics. ii. cells show a scattered response to the DEP field.

to testing, cell appearances were captured with an integrated microscope camera. Figure 4.4 shows the resultant normalized $Re(f_{cm})$ value for each test. It is seen that majority of the measurements are in agreement with each other. On the other hand, some measurements appeared high above or low below the average value.

Figure 4.5 shows randomly selected cells from each measurement group, where the upper snapshots correspond to the cells which exhibit average $Re(f_{cm})$ value. On the other hand, the below snapshots correspond to the cells that showed a DEP response with a greater degree of deviation than the average. It is clearly observed that the cells that show scattered DEP response to the applied electric-field appear to have less light intensity than the majority of the population that show similar appearances. Consequently, cell morphology (light intensity and circular shape) was taken into consideration for consistency in the subsequent DEP characterization tests.

4.1.4 The Android Interface and Portable Lab-on-a-chip (LOC) System on K562 cells

As an upgrade to the previous testing method, a lab-on-a-chip (LOC) system was designed, implemented and tested. The LOC system enables stand-alone operation and label-free cell characterization, hence it is portable, low-cost, user-friendly. The

advantages and drawbacks of this system is discussed at the end of this chapter in detail. The LOC system was designed for but not limited to the proposed DEP characterization device. The system consists of a portable signal generator, a CMOS image circuit, and a custom developed Android software, and requires a smartphone as a processor. The signal generator, CMOS imager, software was developed by M. Kamil Aslan.

All design considerations were focused on the portability and stability. For this reason, it is important to utilize a compact signal generator to energize the electrodes inside the microchannel. Therefore, a USB powered signal generator circuitry was designed. The characterization of cancer cells require $20 V_{p-p}$ sinusoidal voltage with varying frequencies and opposite phases. The designed signal generator circuit is composed of ATmega microcontroller, 6009 DC to DC boost circuitry, AD9850 waveform generator integrated circuit (IC), and an adjustable voltage amplifier stage. The sinusoidal voltages with 180° phase difference was generated by the waveform generator IC. Arduino board was used in programming the microcontroller in order to have control on the output frequency between 1 kHz and 50 MHz. Generated sinusoidal signals were amplified to $20 V_{p-p}$ via voltage amplifier with single supply OPAMP configuration. The OPAMP was biased through DC supply voltage of the USB Interface (5V) boosted using XL 6009 IC. The picture of the signal generator circuit and schematics are shared in Figure 4.6.

Cell motion was captured via GC308, a commercial CMOS image sensor. The field-of-view (FoV) of the image sensor is 3.7 mm^2 , sufficient to capture active analysis area of the microchannel. The sensor has a pixel dimensions of $3.4 \mu\text{m} \times 3.4 \mu\text{m}$, providing sufficient resolution for imaging both MCF-7 and K562 cancer cell lines (the limitation and improvement suggestions are discussed at the end of the chapter).

In order to build up a compact structure, a 3-D printed holder was designed and fabricated. Figure 4.7 shows the images of holder and Android Software. The software was uploaded to a smartphone connected to the LOC system via a USB cable to communicate with the CMOS imager and to supply power to the LOC system.

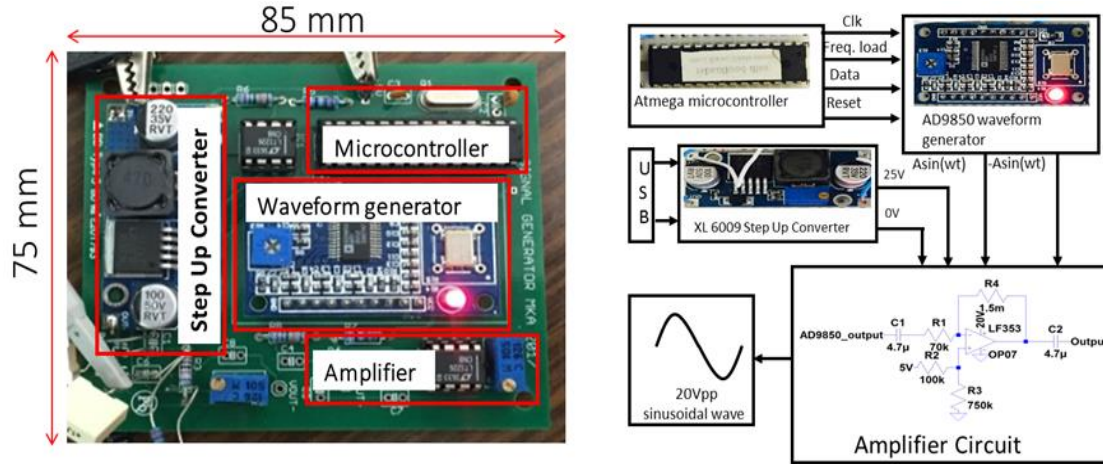


Figure 4.6 Signal generator circuit including ATmega microcontroller, 6009 DC to DC boost circuitry and AD9850 waveform generator IC. Also, an adjustable voltage amplifier stage was implemented. Sinusoidal voltages with 180° phase difference was generated by AD9850 IC. The microcontroller was programmed via Arduino board to control the frequency of the generated sinusoidal voltage between 0 and 50 MHz. Generated signals were amplified to 20 Vp-p employing voltage amplifier with single supply OPAMP configuration. DC supply voltage of the USB interface (5V) was boosted using XL 6009 IC to bias the OPAMPs.

The workflow of the LOC system is summarized below.

Video Capturing

The frames were recorded with CMOS image sensor and transferred to the smartphone memory drive via UVC (USB Video Class) interface at 30 fps in order to obtain the cell motion under the influence of the DEP field.

Frame Enhancement

Recorded cell video was recalled from the application and sampled into frames. The frames were converted to grey scale. In order to eliminate the pixel noise, Gaussian blurring algorithm with 2×2 kernel size was applied.

Cell tracking

Canny Edge Detection was used to identify circle-like objects, where segmented edges were fixed with image filling operation. Image opening operation was applied in order to

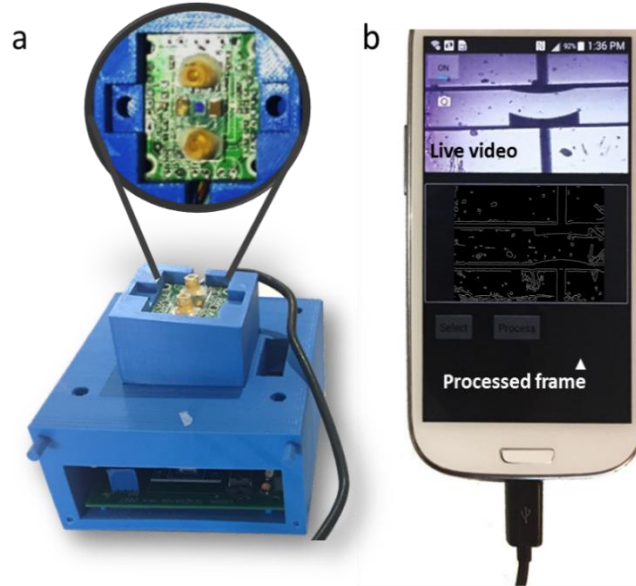


Figure 4.7 LOC system. (a) CMOS image sensor and DEP device placed with-in 3-D printed holder connected to a smartphone via micro-USB connection. Portable signal generator circuit mounted in 3-D printed holder to generate two sinusoidal signals with 180_{phase} difference at desired frequency. (b) Custom-developed Android software. It is used to communicate with CMOS image sensor and conduct frame by frame investigation.

remove the over-segmented regions. The images were approximated to circular shapes and size based elimination was applied to discard the out-of-scope objects (dust, pixel defects etc.) Spatial relationship algorithm was used to track cell positions each frame. The process snapshots is shared in Figure 4.8.

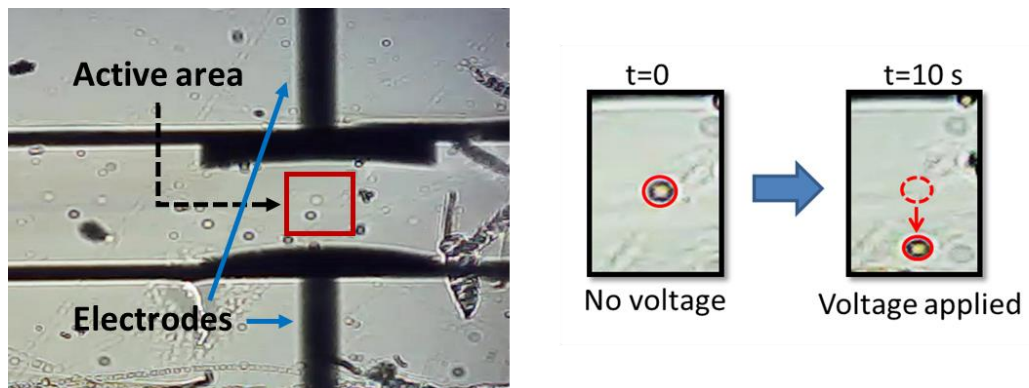


Figure 4.8 Processed image at $t=0$ and $t=10$ s, where cell is attracted towards the concave electrode under the influence of positive DEP force field.

Data Extraction and Velocity Fitting

Center coordinates of each tracked cell and cell radius were recorded into a matrix in terms of microns for each frame. The coordinate flow through frame progress was fitted into a third order polynomial and differentiated by time lapse (calculated by 1/fps). The fitted electric-field simulation data was inserted to the device. Similar to MATLAB program, using velocity, radius and $\nabla|\vec{E}|^2$ data in Equation (18), average Clausius-Mossotti factor for each cell at a frequency was calculated.

4.2 Results

In this study a DEP characterization system is proposed, in which the system can characterize dielectric cells in order to obtain $Re(f_{cm})$ and frequency relationship. 15 different frequency values were tested between 30 kHz and 50 MHz for both MCF-7 and K562 cells. At each frequency 10 different cells cultured in three different populations were examined. The minimum and maximum frequency values were selected according to a saturated response and signal generator limitations respectively. According to the availability MATLAB based post processing corresponds to the MCF-7 cell investigation and portable LOC system was used in characterizing K562 cells.

Before sharing the results it is essential to first verify the constructed theory and analysis methodology.

4.2.1 Experimental Verification

This section is very important for the sake of completeness of the thesis and the success of the proposal. Since cells exhibit dynamic dielectric behaviors we already discussed the error that is caused by the cell modelling results. The main objective of this thesis study was to achieve an accurate dielectric characterization.

In order to verify the proposed analysis methodology initial results were gathered. According to the theoretical model in this study (Sections 2.3 and 3.3), DEP force should be encountered by the drag force, resulting in a balance of the forces on particle. With this assumption, Equation (18) was obtained after going through aforementioned algebra. Since all of the components except particle velocity, u_{px} , and electric field gradient, $\nabla|E|^2$ are constant in Equation (18), for the assumption to be true, these two factors should be linearly dependent to each other.

In order to test this, cell motion under the influence of a DEP force was recorded when 20 V_{p-p} at 1 MHz applied to the electrodes. The velocity was calculated in MATLAB and velocity vs. $\nabla|E|^2$ graph was obtained. The graph is shared in Figure 4.9. It is seen that, as the model suggests, cell velocity follows the $\nabla|E|^2$ value, verifying the initial assumption. This also shows the importance of the uniformity of $\nabla|\vec{E}|^2$ since, cell velocity could not catch the force field in other cases.

After verification of the initial assumption, the tests were continued to obtain $Re(f_{cm})$ vs. frequency of both cell groups.

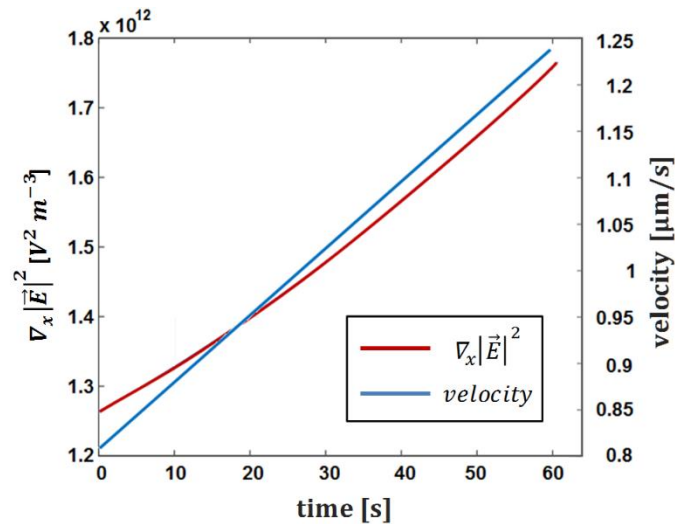


Figure 4.9 Comparison of cell velocity and generated electric field gradient at cell's position. As expected, cell velocity is directly related to the electric field gradient curve, hence $Re(f_{cm})$ value becomes position and time independent.

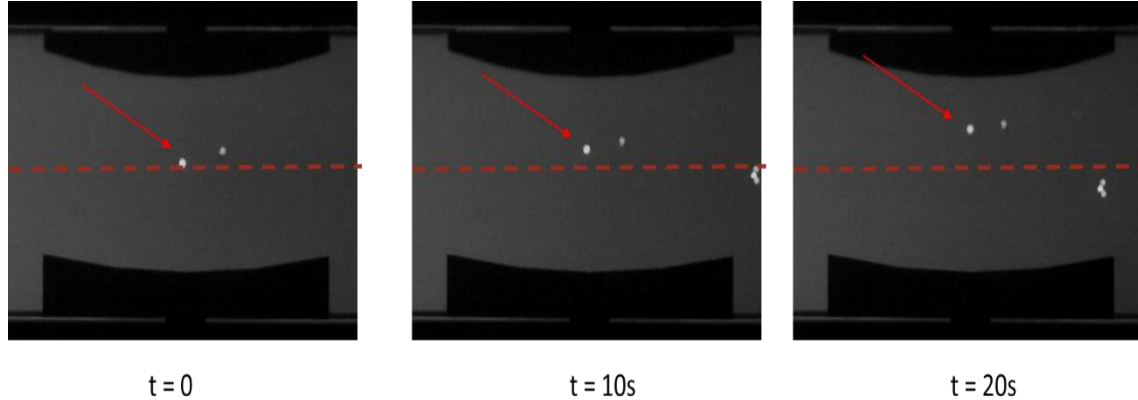


Figure 4.10 Snapshots corresponding to the experiment on MCF-7 cells at 1 MHz, taken at different time intervals. It is seen that under the influence of a DEP force MCF-7 cells start to move towards the convex electrode.

4.2.2 Test Results on MCF-7 cells

XX shows the snapshots of a randomly selected experiment on a MCF-7 cell at 1 MHz. It is observed that at this frequency MCF-7 cell started to be pulled towards convex electrode under the influence of positive DEP force. After completing the measurements at a variety of frequencies both cross-over frequencies corresponding to the transition points between negative DEP and positive DEP regions were found. These cross-over frequencies were recorded as 107 kHz and 35.4 MHz, respectively for negative to positive transition and positive to negative transition, as shared in Figure 4.11. According to the MCF-7 results, After 107 kHz particles start to experience a positive DEP force and were pulled towards the convex electrode. This behaviors proceeds until 35.4 MHz, in which particles feel zero force at that particular frequency.

4.2.3 Test Results on K562 cells

Using Eqn. 18, $Re(f_{cm})$ value was calculated for each frequency stop. Two transition points between negative and positive DEP regions were observed, appearing at 200 kHz and 39.8 MHz, respectively as shown in Figure 4.12. The system measures the average K562 cell radius as 5.87 μm .

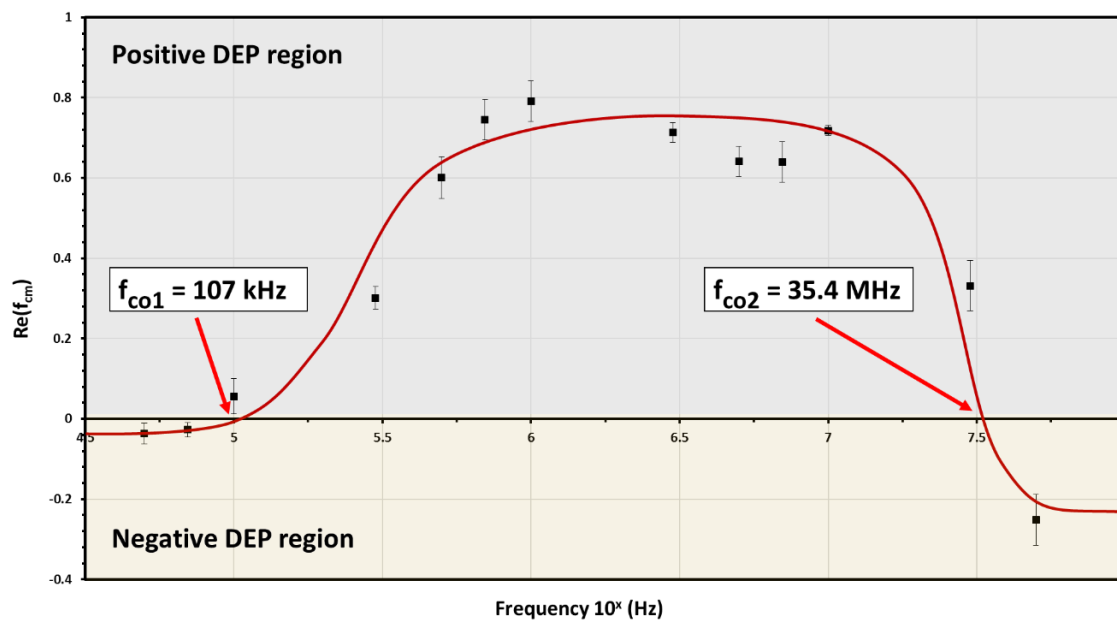


Figure 4.11 DEP Spectrum of MCF7 cells. Cross-over frequencies were found as 107 kHz and 35.4 MHz. Between these frequencies, cells are attracted to denser electric-field regions (positive DEP).

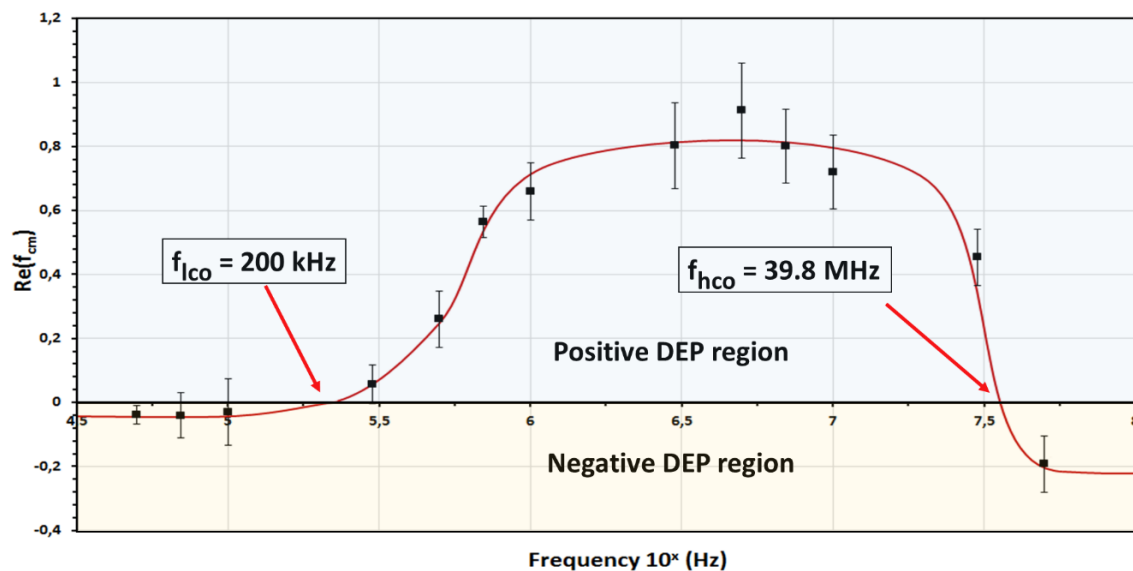


Figure 4.12 DEP spectrum results of K562 Myelogenous leukemia cell line. The cross-over frequencies appeared at 200 kHz and 39.8 MHz. In addition, cells experienced lower magnitude of negative DEP force compared to positive DEP force.

4.3 Discussion

The introduced system in this thesis can be used for direct dielectrophoretic characterization of various cancer cell lines, which will act as a potential tool to increase operation efficiency of cell separation systems that rely on DEP [43]. Studies that uses DEP to assess cancer in clinical samples report separation efficiency up to a limited level. For instance, Gupta et al. reported maximum recovery as 80% for SKOV3 cells and 76.2% for MDA-MB-231 cells from 7.5 ml of normal human donor blood [50]. In another study, mean value of the spiked cancer cell recoveries were reported as 69.9%, 64.9% and 67.8% for 1000 of A549, ASPS-1 and MDA-MB-231 cells per 10^7 PBMCs respectively [51]. These efficiencies are still far from meeting the medical requirements for early cancer detection, as these cells are so rare (1-3 cells per 10^9 blood cells) [42], [82]. Hence, it is still very critical to increase the operation efficiency of current DEP separation systems. The main reason for low-throughput in DEP devices is the relatively low DEP forces affecting the cells. Dielectric properties of the suspending DEP medium and the frequency of the applied voltage are important design considerations in order to increase the relative DEP force (i.e. to obtain a condition where both target and adjacent cells are under influence of a high DEP force but in opposite directions) [43], [61]–[63], [65]. The DEP characterization system allows to test different operating conditions and obtain the DEP characteristics of different cell lines for each condition. Therefore, it can be used in DEP systems prior to separation tests to acquire the optimum experimental conditions in which the relative DEP force is maximum.

4.3.1 *Experimental Drawbacks and Applied Solutions*

There are certain limitations and problems that occurs in the experimental procedure. This section is dedicated to discuss the problems that were encountered, applied and proposed solutions.

The major issue in the field of oncology is that cell have dynamic behaviors [43], [44]. This means, both the physiological (size, shape, color, permeability, density) and the

electrical (membrane permittivity and conductivity, cytoplasmic permittivity and conductivity, ion balances) cell properties may alter in time. The main idea of the system proposed in this thesis is to obtain DEP behavior of cancer cells without creating dependency on electrical cell behaviors. Therefore, a DEP separation system can separate any cell group by initially running this characterization process proposed by this thesis. On the other hand, cells have a certain life cycle and their viability is dependent on the environmental conditions. Since viability directly affects the selective permeability of the cell wall, ionic balances hence the DEP characteristics are affected. In addition, the physical properties such as brightness and compact shape are affected by the cell life cycle. Therefore, in order to be clinically used the tests should be conducted with viable cells. In order to identify the relation between the cell morphology (therefore cell viability) and the DEP characteristics an initial DEP characterization test at 1 MHz was conducted and a relation between cell appearance and DEP stability was established to form a ground basis for the target cells in the future tests.

One major drawback in the testing is the quality of the cultured cell solution. Figure 4.13 shows two different cell culturing cases that were introduced to the channel. Dead cells bring residual sediments and therefore creates physical obstacles that prevents fine cell flow. In addition, some sediments cannot be removed from channel through flushing, and requires disposal of the device. In order to decrease the number of dead cells inside the final solution that is to be introduced to the microchannel, several tests were conducted in the centrifuge steps until the optimum centrifuge spin-force was obtained. In addition prior to the injection stage, a viability test was applied to the solution. An example test result is shared in Figure 4.14. A minimum of 95% viability was conditioned for the testing to start.

For the analysis it is required that the solution should be stationary. Since the proposed DEP characterization devices were designed in a microchannel form, the flow rate can be controlled by the inlet and outlet pressures. However, due to the fact that the channel dimensions as well as inlet and outlet port sizes are in micron range, the minuscule

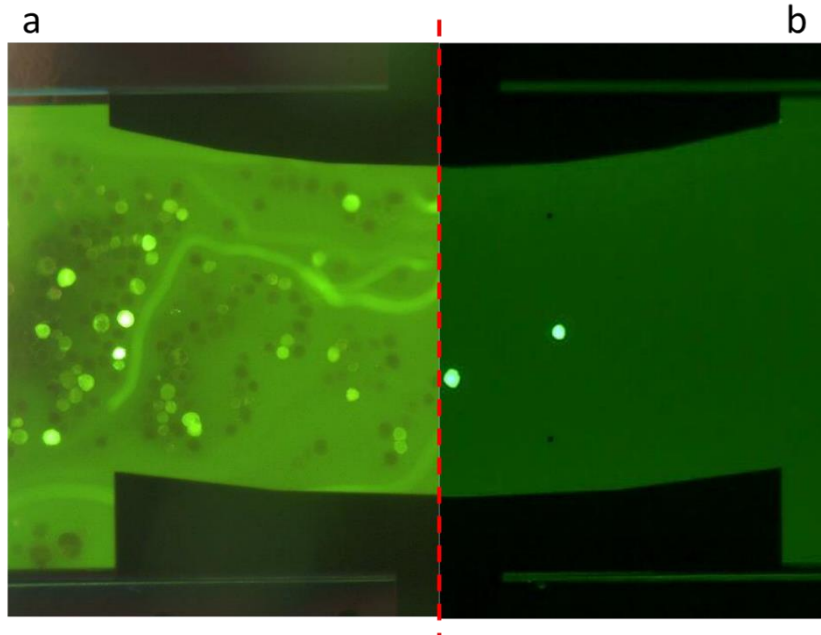


Figure 4.13 Microscopy snapshot of the microchannel with two different solutions at two different times. (a) Image corresponding to continuous flow where dead cells dominate the flow and disable successful tests. (b) A pure cell solution with residue-free environment. Notice that the channel only contains live cells.

pressure changes can have huge effects on flow rate, and a delay is observed in the outcome. Theoretically, applying same pressure values to both inlet and outlet ports would lead a force balance, hence fluid should become stationary. On the other hand, the elasticity of parylene-C and the fabrication errors cause micron ranged differences in the inlet and outlet port sizes. This brings a disequilibrium when the exact same pressures are applied. Therefore, arranging the correct pressure values for inlet and outlet values

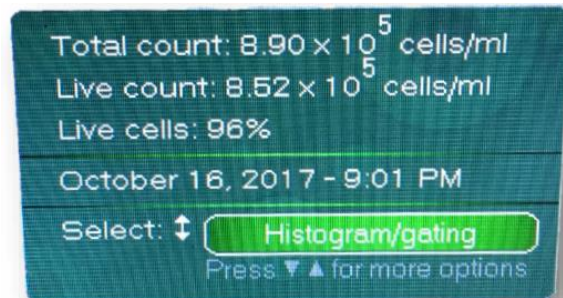


Figure 4.14 Cell count of K562 cells prior to the testing. 96% of the cells are alive. This is a prerequisite for testing to start.

become a time consuming problem. In order to have a more precise control on the flow rate, as discussed before, PDMS channel with a larger inlet and outlet openings were tested. Where instead of applying positive pressure into the inlet port, a reservoir was implemented at the inlet and negative pressure was applied from the outlet. Figure 4.15 shows the application of the proposed method. However, due to sticking problems of PDMS channel on parylene-C layer, this brought different problems. Therefore, this limitation of very high-sensitivity was accepted in this system. If in a future study PDMS-parylene boundary problem will be solved, the fabrication of the DEP characterization devices can be modified accordingly.

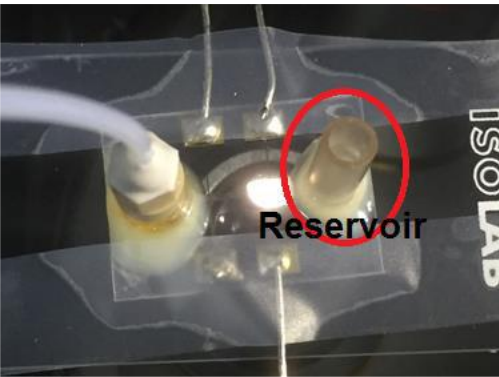


Figure 4.15 Reservoir plantation to the channel inlet.

CHAPTER 5

CONCLUSION AND FUTURE WORK

The main objective of this thesis is to achieve a generic cell characterization system using dielectrophoresis without ascertaining dielectric properties of biological cells. The system presents a novel dielectrophoretic cell analysis technique that obtains $Re(f_{cm})$ data at a single cell level through establishing connection between a strong theory, electric-field simulations and target cell motion. Cell dielectric properties are not used in the analysis and calculations, hence errors caused by cell electric property and cell modelling assumptions are minimized. The utilized electrode structure inside the microfluidic channel provides isomotive electric field, hence it is possible to relate $\nabla|\vec{E}|^2$ field experienced by the target cell and the cell velocity to obtain a meaningful $Re(f_{cm})$ value. The introduced system can be integrated to the cell separation systems that rely on DEP in order to obtain the optimum operating conditions and therefore increase the operation efficiency. This is very critical since current cancer detection efficiencies are far from meeting the medical requirements.

In order to understand the dielectrophoretic behaviour (behaviour under the influence of a non-uniform electric field) of a living organism, DEP characterization devices were designed, simulated and analysed. The system was tested with both MCF-7 and K562 cell types and results show a low deviation as well as cross-correlation with the literature.

The proposed system has several advantages over conventional DEP cytometry methods. First of all, the system does not contain bulky equipment such as microscope, desktop

signal generator or a computer, therefore it provides cost-effective and portable operation. The portability allows that the system can be used at point-of-care without the necessity of fully equipped laboratory, especially in many resource limited regions [83]. Moreover, the use of Android application, CMOS image sensor, and a portable signal generator enables automation together with label- and lens-free operation for single cell level analysis. Therefore, minimally trained persons can use the system with the minimum effort and human based errors and biases are minimized. This feature increases the easy-to-use ability and robustness of the system. In addition, Android is an open source platform and can easily be adapted (supports various programming languages and tools) for possible future version upgrades and code modifications. The proposed technique used in the Clausius-Mossotti factor calculations is also novel, where the factor is directly obtained without ascertaining cell dielectric properties. The performance of the system is limited with the throughput (5 cells can be analysed simultaneously) and resolution of the CMOS image sensor. However, the throughput of the system can be increased by updating the design parameters, and by introducing array-based multichannel approach. In addition, resolution will not introduce any problem considering the size of the analysed cells. For the extreme cases, where cells have smaller sizes ($\sim 1 \mu\text{m}$ in diameter), with the implementation of CMOS image sensor having smaller pixel size or by using image reconstruction algorithms, resolution can be improved [84]–[86].

In addition to minor upgrades in the system to obtain more a more generic operation, as a future work, a cell characterization system can be constructed and optimized based on this study. Since, cancer cell types are showing deviation and demonstrating a dynamic behaviour, the best way to verify this system is to use it in an actual DEP based cell separation system. The system is a low-cost transportable DEP cytometer that could have all sorts of applications. Therefore it can be modified for a very wide range of applications, some of which may be cancer but not limited to, for a future work.

REFERENCES

- [1] World Health Organisation (WHO), “A report about cancer,” 2018. [Online]. Available: <http://www.who.int/news-room/fact-sheets/detail/cancer>.
- [2] B. W. Stewart and C. P. Wild, “World cancer report 2014,” *World Health Organization*, pp. 1–2, 2014.
- [3] C. Desantis, J. Ma, L. Bryan, and A. Jemal, “Breast Cancer Statistics , 2013,” *CA Cancer Journal for Clinicians*, vol. 64, no. 1, pp. 52–62, 2013.
- [4] A. B. Miller, C. J. Baines, T. To, and C. Wall, “Canadian National Breast Screening Study: 1. Breast cancer detection and death rates among women aged 40 to 49 years.,” *CMAJ: Canadian Medical Association journal = journal de l’Association medicale canadienne*, vol. 147, no. 10, pp. 1459–1476, 1992.
- [5] J. D. Schiffman, P. G. Fisher, and P. Gibbs, “Early detection of cancer: past, present, and future,” *Am Soc Clin Oncol Educ Book*, pp. 57–65, 2015.
- [6] M. Porta, *A dictionary of epidemiology*. Oxford University Press, 2014.
- [7] K. E. Petersen, “Silicon as a mechanical material,” *Proceedings of the IEEE*, vol. 70, no. 5, pp. 420–457, 1982.
- [8] K. D. Wise and K. Najafi, “Microfabrication techniques for integrated sensors and microsystems,” *Science*, vol. 254, no. 5036, pp. 1335–1342, 1991.
- [9] B. R. Smith, M. Ruegsegger, P. A. Barnes, M. Ferrari, and S. C. Lee, “Nanodevices in biomedical applications,” in *BioMEMS and Biomedical Nanotechnology*, Springer, 2006, pp. 363–398.
- [10] K. C. Neuman and A. Nagy, “Single-molecule force spectroscopy: optical tweezers, magnetic tweezers and atomic force microscopy,” *Nature methods*, vol.

5, no. 6, p. 491, 2008.

- [11] A. Ashkin, J. M. Dziedzic, J. E. Bjorkholm, and S. Chu, "Observation of a single-beam gradient force optical trap for dielectric particles," *Optics letters*, vol. 11, no. 5, pp. 288–290, 1986.
- [12] E. Eriksson *et al.*, "A microfluidic device for reversible environmental changes around single cells using optical tweezers for cell selection and positioning," *Lab on a Chip*, vol. 10, no. 5, pp. 617–625, 2010.
- [13] S. Dochow *et al.*, "Tumour cell identification by means of Raman spectroscopy in combination with optical traps and microfluidic environments," *Lab on a Chip*, vol. 11, no. 8, pp. 1484–1490, 2011.
- [14] M. M. Wang *et al.*, "Microfluidic sorting of mammalian cells by optical force switching," *Nature biotechnology*, vol. 23, no. 1, p. 83, 2005.
- [15] M. Stephens, M. S. Talary, R. Pethig, A. K. Burnett, and K. I. Mills, "The dielectrophoresis enrichment of CD34+ cells from peripheral blood stem cell harvests.," *Bone marrow transplantation*, vol. 18, no. 4, pp. 777–782, 1996.
- [16] P. H. Shih, J.-Y. Shiu, P.-C. Lin, C.-C. Lin, T. Veres, and P. Chen, "On chip sorting of bacterial cells using sugar-encapsulated magnetic nanoparticles," *Journal of Applied Physics*, vol. 103, no. 7, p. 07A316, 2008.
- [17] J. H. Kang, S. Krause, H. Tobin, A. Mammoto, M. Kanapathipillai, and D. E. Ingber, "A combined micromagnetic-microfluidic device for rapid capture and culture of rare circulating tumor cells," *Lab on a Chip*, vol. 12, no. 12, pp. 2175–2181, 2012.
- [18] K. Hoshino *et al.*, "Microchip-based immunomagnetic detection of circulating tumor cells," *Lab on a Chip*, vol. 11, no. 20, pp. 3449–3457, 2011.

- [19] K. H. Han and A. B. Frazier, "Paramagnetic capture mode magnetophoretic microseparator for high efficiency blood cell separations," *Lab on a Chip*, vol. 6, no. 2, pp. 265–273, 2006.
- [20] G. M. Whitesides, "The origins and the future of microfluidics," *Nature*, vol. 442, no. 7101, p. 368, 2006.
- [21] S. Choi, S. Song, C. Choi, and J. Park, "Sheathless focusing of microbeads and blood cells based on hydrophoresis," *Small*, vol. 4, no. 5, pp. 634–641, 2008.
- [22] D. Di Carlo, D. Irimia, R. G. Tompkins, and M. Toner, "Continuous inertial focusing, ordering, and separation of particles in microchannels," *Proceedings of the National Academy of Sciences*, vol. 104, no. 48, pp. 18892–18897, 2007.
- [23] S. C. Hur, N. K. Henderson-MacLennan, E. R. B. McCabe, and D. Di Carlo, "Deformability-based cell classification and enrichment using inertial microfluidics," *Lab on a Chip*, vol. 11, no. 5, pp. 912–920, 2011.
- [24] R. M. Hochmuth, "Micropipette aspiration of living cells," *Journal of biomechanics*, vol. 33, no. 1, pp. 15–22, 2000.
- [25] W. A. Bonner, H. R. Hulett, R. G. Sweet, and L. A. Herzenberg, "Fluorescence Activated Cell Sorting," *Review of Scientific Instruments*, vol. 43, no. 3, p. 404, 1972.
- [26] A. Rembaum, R. C. K. Yen, D. H. Kempner, and J. Ugelstad, "Cell labeling and magnetic separation by means of immunoreagents based on polyacrolein microspheres," *Journal of Immunological Methods*, vol. 52, no. 3, pp. 341–351, 1982.
- [27] S. Miltenyi, W. Müller, W. Weichel, and A. Radbruch, "High gradient magnetic cell separation with MACS.," *Cytometry*, vol. 11, no. 2, pp. 231–238, 1990.

- [28] J. Zhou, M. Liu, R. Aneja, R. Chandra, H. Lage, and H. C. Joshi, "Reversal of P-glycoprotein-mediated multidrug resistance in cancer cells by the c-Jun NH₂-terminal kinase," *Cancer Research*, vol. 66, no. 1, pp. 445–452, 2006.
- [29] M. P. Hughes, "Fifty years of dielectrophoretic cell separation technology," *Biomicrofluidics*, vol. 10, no. 3, pp. 1–9, 2016.
- [30] J. Voldman, "Electrical Forces for Microscale Cell Manipulation," *Annual Review of Biomedical Engineering*, vol. 8, no. 1, pp. 425–454, 2006.
- [31] R. Pethig and G. H. Markx, "Applications of dielectrophoresis in biotechnology," *Trends in Biotechnology*, vol. 15, no. 10, pp. 426–432, 1997.
- [32] C. M. Das, F. Becker, S. Vernon, J. Noshari, C. Joyce, and P. R. C. Gascoyne, "Dielectrophoretic Segregation of Different Human Cell Types on Microscope Slides Dielectrophoretic Segregation of Different Human Cell Types on Microscope Slides," *Analytical Chemistry*, vol. 77, no. 9, pp. 2708–2719, 2005.
- [33] H. A. Pohl, "The Motion and Precipitation of Suspensoids in Divergent Electric Fields," *Journal of Applied Physics*, vol. 22, no. 7, p. 869, 1951.
- [34] M. Elitas, R. Martinez-Duarte, N. Dhar, J. D. McKinney, and P. Renaud, "Dielectrophoresis-based purification of antibiotic-treated bacterial subpopulations.," *Lab on a chip*, vol. 14, no. 11, pp. 1850–1857, 2014.
- [35] G. H. Markx, Y. Huang, X.-F. Zhou, and R. Pethig, "Dielectrophoretic characterization and separation of micro-organisms," *Microbiology*, vol. 140, pp. 585–591, 1994.
- [36] G. H. Markx, P. A. Dyda, and R. Pethig, "Dielectrophoretic separation of bacteria using a conductivity gradient," *Journal of Biotechnology*, vol. 51, no. 2, pp. 175–180, 1996.

- [37] A. Sonnenberg *et al.*, “Dielectrophoretic Isolation and Detection of cfc-DNA Nanoparticulate Biomarkers and Virus from Blood,” *Electrophoresis*, vol. 34, no. 7, pp. 1076–1084, 2013.
- [38] M. Alshareef *et al.*, “Separation of tumor cells with dielectrophoresis-based microfluidic chip,” *Biomicrofluidics*, vol. 7, no. 1, 2013.
- [39] F. F. Becker, X. Wang, Y. Huang, R. Pethigt, J. Vykoukal, and P. R. C. Gascoyne, “Separation of human breast cancer cells from blood by differential dielectric affinity,” vol. 92, no. January, pp. 860–864, 1995.
- [40] Y. Demircan, A. Koyuncuoglu, M. Erdem, E. Ozgur, U. Gunduz, and H. Kulah, “Label-free detection of multidrug resistance in K562 cells through isolated 3D-electrode dielectrophoresis,” *Electrophoresis*, vol. 36, no. 9–10, pp. 1149–1157, 2015.
- [41] M. S. Talary, K. I. Mills, T. Hoy, a K. Burnett, and R. Pethig, “Dielectrophoretic separation and enrichment of CD34+ cell subpopulation from bone marrow and peripheral blood stem cells.,” *Medical {&} biological engineering {&} computing*, vol. 33, no. 2, pp. 235–237, 1995.
- [42] A. Lucci *et al.*, “Circulating tumour cells in non-metastatic breast cancer: A prospective study,” *The Lancet Oncology*, vol. 13, no. 7, pp. 688–695, 2012.
- [43] Y. Demircan, E. Ozgur, and H. Kulah, “Dielectrophoresis: Applications and future outlook in point of care,” *Electrophoresis*, vol. 34, no. 7, pp. 1008–1027, 2013.
- [44] Z. R. Gagnon, “Cellular dielectrophoresis: Applications to the characterization, manipulation, separation and patterning of cells,” *Electrophoresis*, vol. 32, no. 18, pp. 2466–2487, 2011.
- [45] Y. Li and K. V. I. S. Kaler, “Dielectrophoretic fluidic cell fractionation system,” *Analytica Chimica Acta*, vol. 507, no. 1, pp. 151–161, 2004.

- [46] H. A. Pohl, “Dielectrophoresis,” *The behavior of neutral matter in nonuniform electric fields*, 1978.
- [47] X. Hu, W. M. Arnold, and U. Zimmermann, “Alterations in the electrical properties of T and B lymphocyte membranes induced by mitogenic stimulation. Activation monitored by electro-rotation of single cells,” *Biochimica et Biophysica Acta*, vol. 1021, no. 2, pp. 191–200, 1990.
- [48] I. Ermolina and H. Morgan, “The electrokinetic properties of latex particles: Comparison of electrophoresis and dielectrophoresis,” *Journal of Colloid and Interface Science*, vol. 285, no. 1, pp. 419–428, 2005.
- [49] S. Shim, K. Stenke-Hale, J. Noshari, F. F. Becker, and P. R. C. C. Gascoyne, “Dielectrophoresis has broad applicability to marker-free isolation of tumor cells from blood by microfluidic systems,” *Biomicrofluidics*, vol. 7, no. 1, 2013.
- [50] V. Gupta *et al.*, “ApoStreamTM, a new dielectrophoretic device for antibody independent isolation and recovery of viable cancer cells from blood,” *Biomicrofluidics*, vol. 6, no. 2, p. 24133, 2012.
- [51] P. Balasubramanian *et al.*, “Antibody-independent capture of circulating tumor cells of non-epithelial origin with the ApoStream[®] system,” *PloS one*, vol. 12, no. 4, p. e0175414, 2017.
- [52] F. H. Labeed, H. M. Coley, H. Thomas, and M. P. Hughes, “Assessment of multidrug resistance reversal using dielectrophoresis and flow cytometry.,” *Biophysical journal*, vol. 85, no. 3, pp. 2028–2034, 2003.
- [53] E. A. Henslee, M. B. Sano, A. D. Rojas, E. M. Schmelz, and R. V. Davalos, “Selective concentration of human cancer cells using contactless dielectrophoresis,” *Electrophoresis*, vol. 32, no. 18, pp. 2523–2529, 2011.
- [54] J. An, J. Lee, S. H. Lee, J. Park, and B. Kim, “Separation of malignant human breast

cancer epithelial cells from healthy epithelial cells using an advanced dielectrophoresis-activated cell sorter (DACS),” *Analytical and bioanalytical chemistry*, vol. 394, no. 3, pp. 801–809, 2009.

- [55] B. Cetin and D. Li, “Dielectrophoresis in microfluidics technology,” *Electrophoresis*, vol. 32, no. 18, pp. 2410–2427, 2011.
- [56] L. L. Gary, *Advanced transport phenomena: fluid mechanics and convective transport processes*. 2007.
- [57] M. Amin, P. P. Dey, and H. Badkoobehi, “A complete electrical equivalent circuit model for biological cell A Complete Electrical Equivalent Circuit Model For Biological Cell,” no. April 2008, 2015.
- [58] A. H. Kyle, C. T. O. Chan, and A. I. Minchinton, “Characterization of Three-Dimensional Tissue Cultures Using Electrical Impedance Spectroscopy,” *Biophysical Journal*, vol. 76, no. 5, pp. 2640–2648, 1999.
- [59] R. J. Liedtke, “The fundamentals of bioelectrical impedance analysis,” *RJL Systems*: http://www.rjlsystems.com/docs/bia_info/fundamentals/fundamentals.pdf, 1998.
- [60] M. Amin, “Phase characteristics of a three component lipid system in aqueous electrolyte solution,” 1985.
- [61] R. Pethig, “Dielectrophoresis: Status of the theory, technology, and applications,” *Biomicrofluidics*, vol. 4, no. 2, 2010.
- [62] C. Huang, C. Liu, J. Loo, T. Stakenborg, and L. Lagae, “Single cell viability observation in cell dielectrophoretic trapping on a microchip,” *Applied Physics Letters*, vol. 104, no. 1, 2014.
- [63] P. R. C. Gascoyne, J. Noshari, T. J. Anderson, and F. F. Becker, “Isolation of rare

- cells from cell mixtures by dielectrophoresis,” *Electrophoresis*, vol. 30, no. 8, pp. 1388–1398, 2009.
- [64] Y. Huang, R. Hölzel, R. Pethig, and X. B. Wang, “Differences in the AC electrodynamics of viable and non-viable yeast cells determined through combined dielectrophoresis and electrorotation studies.,” *Physics in medicine and biology*, vol. 37, no. 7, pp. 1499–1517, 1992.
- [65] R. R. Pethig, *Dielectrophoresis: Theory, Methodology and Biological Applications*. John Wiley & Sons, 2017.
- [66] M. B. Sano, E. A. Henslee, E. Schmelz, and R. V. Davalos, “Contactless dielectrophoretic spectroscopy: examination of the dielectric properties of cells found in blood,” *Electrophoresis*, vol. 32, no. 22, pp. 3164–3171, 2011.
- [67] J. An, J. Lee, Y. Kim, B. Kim, and S. Lee, “Analysis of cell separation efficiency in dielectrophoresis-activated cell sorter,” in *Nano/Micro Engineered and Molecular Systems, 2008. NEMS 2008. 3rd IEEE International Conference on*, 2008, pp. 965–969.
- [68] P. R. C. Gascoyne, S. Shim, J. Noshari, F. F. Becker, and K. Stemke-Hale, “Correlations between the dielectric properties and exterior morphology of cells revealed by dielectrophoretic field-flow fractionation,” *Electrophoresis*, vol. 34, no. 7, pp. 1042–1050, 2013.
- [69] H. M. Coley, F. H. Labeed, H. Thomas, and M. P. Hughes, “Biophysical characterization of MDR breast cancer cell lines reveals the cytoplasm is critical in determining drug sensitivity,” *Biochimica et Biophysica Acta - General Subjects*, vol. 1770, no. 4, pp. 601–608, 2007.
- [70] S. Chin, M. P. Hughes, H. M. Coley, and F. H. Labeed, “Rapid assessment of early biophysical changes in K562 cells during apoptosis determined using

- dielectrophoresis,” *international Journal of nanomedicine*, vol. 1, no. 3, p. 333, 2006.
- [71] F. H. Labeed, H. M. Coley, and M. P. Hughes, “Differences in the biophysical properties of membrane and cytoplasm of apoptotic cells revealed using dielectrophoresis,” *Biochimica et Biophysica Acta (BBA)-General Subjects*, vol. 1760, no. 6, pp. 922–929, 2006.
- [72] K. A. Graham *et al.*, “A dielectrophoretic method of discrimination between normal oral epithelium, and oral and oropharyngeal cancer in a clinical setting,” *Analyst*, vol. 140, no. 15, pp. 5198–5204, 2015.
- [73] L. M. Broche, F. H. Labeed, and M. P. Hughes, “Extraction of dielectric properties of multiple populations from dielectrophoretic collection spectrum data,” *Physics in Medicine and Biology*, vol. 50, no. 10, pp. 2267–2274, 2005.
- [74] H. S. Moon *et al.*, “Continuous separation of breast cancer cells from blood samples using multi-orifice flow fractionation (MOFF) and dielectrophoresis (DEP),” *Lab on a Chip*, vol. 11, no. 6, p. 1118, 2011.
- [75] S. B. Huang *et al.*, “High-purity and label-free isolation of circulating tumor cells (CTCs) in a microfluidic platform by using optically-induced-dielectrophoretic (ODEP) force,” *Lab on a Chip*, vol. 13, no. 7, p. 1371, 2013.
- [76] C. Chung, M. Waterfall, S. Pells, A. Menachery, S. Smith, and R. Pethig, “Dielectrophoretic characterisation of mammalian cells above 100 MHz,” *Journal of Electrical Bioimpedance*, vol. 2, no. 1, pp. 64–71, 2011.
- [77] K. Asami, Y. Takahashi, and S. Takashima, “Dielectric properties of mouse lymphocytes and erythrocytes,” *Biochimica et Biophysica Acta (BBA)-Molecular Cell Research*, vol. 1010, no. 1, pp. 49–55, 1989.
- [78] F. Yang, X. Yang, H. Jiang, W. M. Butler, and G. Wang, “Dielectrophoretic

Separation of Prostate Cancer Cells,” *Technology in Cancer Research & Treatment*, vol. 12, no. 1, 2012.

- [79] Z. Çağlayan, K. Sel, Y. D. Yalçın, Ö. Ş. Sukas, and H. Kùlah, “Analysis of the dielectrophoretic (DEP) spectra of biological cells,” in *Solid-State Sensors, Actuators and Microsystems (TRANSDUCERS), 2017 19th International Conference on*, 2017, pp. 1644–1647.
- [80] A. Castellanos, A. Ramos, A. González, N. G. Green, and H. Morgan, “Electrohydrodynamics and dielectrophoresis in microsystems: scaling laws,” *Journal of Physics D: Applied Physics*, vol. 36, no. 20, pp. 2584–2597, 2003.
- [81] F. Du, M. Baune, and J. Thöming, “Insulator-based dielectrophoresis in viscous media-Simulation of particle and droplet velocity,” *Journal of Electrostatics*, vol. 65, no. 7, pp. 452–458, 2007.
- [82] M. Yu, S. Stott, M. Toner, S. Maheswaran, and D. A. Haber, “Circulating tumor cells: approaches to isolation and characterization,” *The Journal of cell biology*, vol. 192, no. 3, pp. 373–382, 2011.
- [83] S. Sharma, J. Zapatero-Rodrìguez, P. Estrela, and R. O’Kennedy, “Point-of-care diagnostics in low resource settings: present status and future role of microfluidics,” *Biosensors*, vol. 5, no. 3, pp. 577–601, 2015.
- [84] T. G. Flohr, K. Stierstorfer, S. Ulzheimer, H. Bruder, A. N. Primak, and C. H. McCollough, “Image reconstruction and image quality evaluation for a 64-slice CT scanner with z-flying focal spot,” *Medical physics*, vol. 32, no. 8, pp. 2536–2547, 2005.
- [85] N. Nguyen, P. Milanfar, and G. Golub, “A computationally efficient superresolution image reconstruction algorithm,” *IEEE transactions on image processing*, vol. 10, no. 4, pp. 573–583, 2001.

- [86] E. McLeod, W. Luo, O. Mudanyali, A. Greenbaum, and A. Ozcan, “Toward gigapixel nanoscopy on a chip: a computational wide-field look at the nano-scale without the use of lenses,” *Lab on a chip*, vol. 13, no. 11, pp. 2028–2035, 2013.
- [87] H. Yun, K. Kim, and W. G. Lee, “Cell manipulation in microfluidics,” *Biofabrication*, vol. 5, no. 2, p. 22001, 2013.
- [88] J. Oblak, D. Križaj, S. Amon, A. Maček-Lebar, and D. Miklavčič, “Feasibility study for cell electroporation detection and separation by means of dielectrophoresis,” *Bioelectrochemistry*, vol. 71, no. 2, pp. 164–171, 2007.